Midshelf to Surfzone Coupled ROMS–SWAN Model Data Comparison of Waves, Currents, and Temperature: Diagnosis of Subtidal Forcings and Response

NIRNIMESH KUMAR AND FALK FEDDERSEN

Scripps Institution of Oceanography, La Jolla, California

YUSUKE UCHIYAMA

Department of Civil Engineering, Kobe University, Kobe, Hyogo, Japan

JAMES MCWILLIAMS

Institute of Geophysics and Planetary Physics, University of California, Los Angeles, Los Angeles, California

WILLIAM O'REILLY

Scripps Institution of Oceanography, La Jolla, California

(Manuscript received 25 July 2014, in final form 9 January 2015)

ABSTRACT

A coupled wave and circulation model that includes tide, wind, buoyancy, and wave processes is necessary to investigate tracer exchange in the shelf region. Here, a coupled Regional Ocean Model System (ROMS)–Simulating Waves Nearshore (SWAN) model, resolving midshelf to the surfzone region of the San Pedro Bay, California, is compared to observations from the 2006 Huntington Beach experiment. Waves are well modeled, and surfzone cross- and alongshore velocities are reasonably well modeled. Modeled and observed rotary velocity spectra compare well in subtidal and tidal bands, and temperature spectra compare well in the subtidal band. Observed and modeled mid- and inner-shelf subtidal velocity ellipses and temperature variability determined from the first vertical complex EOF (cEOF) mode have similar vertical structure. Although the modeled subtidal velocity vertical shear and stratification are weaker than observed, the ratio of stratification to shear is similar, suggesting model vertical mixing is consistent with observations. On fortnightly and longer time scales, the surface heat flux and advective heat flux divergence largely balance on the inner shelf and surfzone. The surfzone and inner-shelf alongshore currents separated by 220 m are unrelated. Both modeled and observed subtidal alongshelf current and temperature are cross-shelf coherent seaward of the surfzone. Wind forcing explains 50% of the observed and modeled inner-shelf alongshore current variability. The observed and modeled inner-shelf alongshelf nonuniformities in depth-averaged alongshore velocities are similar. Inferred, inner-shelf, wave-induced, cross-shore exchange is more important than on the U.S. East Coast. Overall, the coupled ROMS–SWAN model represents well the waves and subtidal circulation dynamics from the midshelf to the surfzone.

1. Introduction

The surfzone (from the shoreline to the seaward extent of depth-limited wave breaking), the inner shelf (from 5- to ≈15-m depths where the surface and bottom boundary layers overlap; e.g., Lentz and Fewings 2012), and midshelf (offshore of the inner shelf to ≈50-m depth, where the surface and the bottom boundary layers are distinct; e.g., Austin and Lentz 2002) together represent the transition region from land to the open ocean. This region exchanges a wide variety of tracers. Terrestrial pollutants such as fecal indicator bacteria, pathogens, and human viruses (e.g., Reeves et al. 2004; Grant et al. 2005) enter the surfzone region and are dispersed by cross-shelf exchange. Similarly, nearshore, harmful algal blooms (i.e., red tides) are controlled by cross-shelf nutrient exchange (e.g., Anderson 2009; Omand et al. 2012). Intertidal invertebrate gametes must typically

Denotes Open Access content.

Corresponding author address: N. Kumar, SIO, 9500 Gilman Dr., La Jolla, CA 92093-0209.
E-mail: n2kumar@ucsd.edu.

DOI: 10.1175/JPO-D-14-0151.1

make their way from near the shoreline to much deeper waters (such as Donax clams; e.g., Laudien et al. 2001; Martel and Chia 1991), while the larvae must be transported onshore for recruitment in the intertidal zone (e.g., Shanks et al. 2010). Surfzone (Sinnett and Feddersen 2014) and inner-shelf (e.g., Fewings and Lentz 2011) temperature fluctuations are influenced by cross-shelf advective heat fluxes. Yet, the exchange of tracers (pollutants, nutrients, larvae, heat, etc.) spanning the surfzone through the midshelf is poorly understood.

Surfzone, inner shelf, and midshelf regions span drastically different dynamical regimes, with varying cross-shelf exchange processes due to wave, wind, buoyancy, and tidal forcing. Within the surfzone, horizontal eddies generated due to short-crested wave breaking (Clark et al. 2012; Feddersen 2014) induce cross-shore dye and drifter dispersion (Spydell et al. 2009; Clark et al. 2010). Surfzone, onshore, wave-induced mass flux is balanced by the offshore-directed undertow, which because of their different vertical structure can lead to cross-surfzone exchange (e.g., Garcez Faria et al. 2000; Reniers et al. 2004; Uchiyama et al. 2010; Kumar et al. 2012). Bathymetrically controlled (e.g., Reniers et al. 2009) and transient rip currents (e.g., Johnson and Pattiaratchi 2006) can also result in surfzone inner-shelf exchange. On an alongshore uniform beach, transient rip currents were the dominant surfzone to inner-shelf dye exchange mechanism (Hally-Rosendahl et al. 2014).

In the inner-shelf region, internal waves affect cross-shelf exchange. Baroclinic semidiurnal waves in the inner shelf (20-m depth) flux heat and nitrate farther inshore (Lucas et al. 2011; Wong et al. 2012). Internal wave mixing is responsible for pumping nutrients up into the euphotic zone, initiating phytoplankton blooms (Omand et al. 2012). Nonlinear internal waves (e.g., Pineda 1994; Nam and Send 2011) can advect cold waters from 6-m depth into the surfzone (Sinnett and Feddersen 2014) and are hypothesized to transport larvae onshore for recruitment (e.g., Pineda 1999).

At subtidal ($\geq$33 hr) time scales, alongshelf, wind-driven upwelling and downwelling controls cross-shelf transport in the midshelf, where surface and bottom boundary Ekman layers do not overlap (Austin and Lentz 2002). However, in the inner shelf, surface and bottom boundary layers overlap, significantly reducing cross-shelf transport (Austin and Lentz 2002; Kirincich and Barth 2009). Nonetheless, inner-shelf cross-shelf currents can be driven by cross-shelf wind forcing (Tilburg 2003; Fewings et al. 2008). Outer shelf surface waters can intrude into the inner shelf from submesoscale activity or interaction with an upwelling front resulting in cross-shelf transport (e.g., Nidzieko and Largier 2013). The inner-shelf undertow due to surface gravity wave–induced, onshore, Stokes drift drives subtidal cross-shelf exchange especially during periods of weak winds and strong wave forcing (Lentz et al. 2008; Kirincich et al. 2009). Also, intrinsic variability due to meso- and submesoscale activity can lead to cross-shore eddy fluxes (Capet et al. 2008; Dong et al. 2009; Romero et al. 2013; Uchiyama et al. 2014, hereinafter U14).

Recent circulation modeling studies have simulated cross-shelf exchange. For example, Romero et al. (2013) applied the Regional Ocean Modeling System (ROMS) to characterize horizontal relative dispersion as a function of coastal geometry, bathymetry, and eddy kinetic energy in the Southern California Bight (SCB). Dispersal and dilution of an outer-shelf (water depth of 60 m) urban wastewater discharge in the San Pedro Bay (SPB) were simulated with ROMS to identify the possibility of contamination in water depth $<$10 m (U14). Harmful algal bloom transport from the outer to midshelf due to wind-driven currents was studied in the Salish Sea using ROMS (Giddings et al. 2014). However, inner-shelf processes were coarsely resolved in these studies, and wave-driven processes were neglected. Surfzone modeling studies typically do not include the inner-shelf, rotational, tidal, and buoyancy effects (e.g., Ruessink et al. 2001; Reniers et al. 2009; Feddersen et al. 2011; Castelle et al. 2014). However, the tracer in this region responds to the net effect of all these surfzone to midshelf processes. A coupled wave and circulation model with wind, wave, tide, and buoyancy forcing and sufficient resolution is required to accurately simulate inner-shelf and surfzone processes. Therefore, prior to studying cross-shelf exchange, a model must be concurrently applied from the midshelf to the surfzone and tested against field measurements.

The Coupled Ocean–Atmosphere–Wave–Sediment Transport model (COAWST; Warner et al. 2010) that couples ROMS and Simulating Waves Nearshore (SWAN v40.91) models (using the Model Coupling Toolkit) includes the buoyancy-, wind-, tide-, and wave-driven processes (McWilliams et al. 2004) to simulate exchange across all components of the shelf region. The COAWST modeling system has not been extensively tested to simulate currents, waves, and temperature in the shelf region. Here, COAWST (coupled ROMS–SWAN) is applied concurrently from the surfzone to the midshelf region adjacent to Huntington Beach, California, in the San Pedro Bay. Model performance is evaluated by statistical comparison of dense measurement of waves, circulation, and temperature on a 4-km-long cross-shore transect spanning the surfzone to midshelf (section 2a) as part of the August–October 2006 Huntington Beach experiment (HB06).

The model physics, grid setup, and surface and boundary forcing required to simulate the hydrodynamics

during the HB06 experiment are described in section 3. Modeled waves, currents, and temperature from the surfzone to inner and midshelf are compared to observations in sections 4 and 5, with focus on subtidal time scales. Model data comparison at tidal time scales will be considered elsewhere. Subsequently, a range of midshelf to surfzone processes is examined jointly in the model and observations to gain insight of the dynamics across this region. The results are summarized in section 7.

2. Observations and methods

a. *HB06 experiment description*

Currents, waves, temperature, and sea surface elevation were measured from the surfzone to the midshelf adjacent to Huntington Beach, California, as a part of the HB06 experiment (Clark et al. 2010, 2011; Omand et al. 2011, 2012; Nam and Send 2011; Feddersen et al. 2011; Feddersen 2012; Rippy et al. 2013). The shoreline and bathymetry are predominantly alongshore uniform and face ~214° southwest. The coordinate system is defined such that positive cross-shore x and alongshore y are directed onshore and toward the northwest, respectively, with $x = 0$ at the shoreline (see Fig. 1a). The vertical coordinate z is positive upward, with $z = 0$ as the mean sea surface level. The mean water depth is h, such that the seabed is at $z = -h$. The time coordinate t starts from $t = 0$ corresponding to 1 August 2006 (UTC). At all locations (midshelf to surfzone), the bathymetry $h(x, y)$ (Fig. 1) is given by the NOAA tsunami digital elevation model (DEM) with 9-m spatial resolution (Caldwell et al. 2011). Near the surfzone ($x > -120$ m), the cross-shore bathymetry profiles evolved in time (Clark et al. 2010) and often had terraced features not seen in the DEM bathymetry. However, because of the lack of measured bathymetry in the substantial part of the model grids (section 3), the DEM bathymetry is also used in the surfzone for model simulation (Fig. 1c).

Moorings equipped with thermistors and ADCP current meters were deployed on a cross-shore transect in water depths of 26, 20, 10, and 8 m (hereinafter denoted as M26, M20, M10, and M8, respectively) from August to October 2006 (see Fig. 1b and Table 1). Farther inshore in the same cross-shore transect, surfzone frames (M4, M3, and M1.5; Fig. 1c) were deployed in 4-, 3.2-, and 1.4-m mean water depth. Each frame was equipped with a pressure sensor and an acoustic Doppler velocimeter (ADV), measuring pressure, three-dimensional velocities, and bed location, and one or two thermistors (Fig. 1c). At the M1.5 deployment location, the mean (time averaged) water depth was $h = 1.4$ m and varied ± 0.2 m during the 33-day deployment. The actual bathymetry evolves and varies from the DEM. To compare

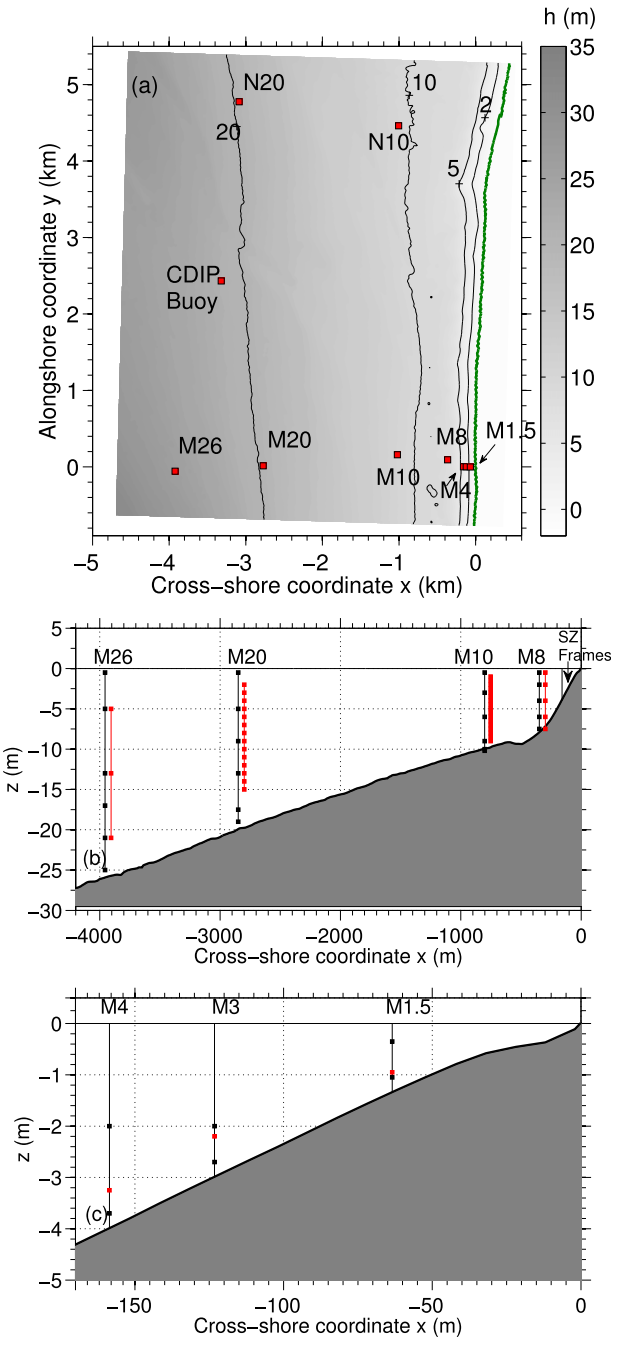

FIG. 1. HB06 instrument schematic: (a) Plan view of bathymetry adjacent to Huntington Beach in the San Pedro Bay, California, with labeled instrument sites (red squares) as a function of cross-shore x and alongshore y coordinates. The green curve represents the zero depth contour ($h = 0$ m). (b) Cross-shore transect at $y = 0$ m of shelf bathymetry on the shelf ($h < 35$ m) and (c) nearshore ($h < 5$ m) with cross-shelf and vertical instrument locations of thermistors (black) and velocity (red) are indicated. The vertical coordinate $z = 0$ m is at mean sea level and positive upward. The bathymetry $h(x, y)$ is from the NOAA tsunami DEM (Caldwell et al. 2011). As surfzone bathymetry was variable, in (c), M1.5 is moved 20 m onshore so that it is in the correct mean water depth.

TABLE 1. List of midshelf to surfzone HB06 experiment cross-shore transect instrument sites, depth, deployment duration, and cross-shore (x) location. The cross-shore location in parentheses for M1.5 is the actual instrument location during the experiment. Here, the surfzone bathymetry is approximate, and the cross-shore location of M1.5 is considered to be 20 m onshore at the same mean water depth $h = 1.4$ m, as observed.

Site	Mean depth (m)	Deployment duration (days)		Cross-shore location (m)
		Temperature	Velocity	
M26	26	86	86	−3950
M20	20	60	86	−2850
M10	10	84	86	−800
M8	8	85	85	−348
M4	4	33	33	−159
M3	3.2	33	33	−123
M1.5	1.4	33	33	−63 (−83)

observed and modeled surfzone waves and currents at the same mean water depth h, the cross-shore location of M1.5 is considered to be 20 m farther onshore from where it was deployed (Fig. 1c).

An additional mooring N10 with an ADCP was deployed in 10-m depth approximately 4 km northwest of the primary cross-shore transect (Figs. 1a,b). A Coastal Data Information Program (CDIP) directional wave buoy (Fig. 1a) deployed in 22-m water depth provided spectral wave estimates, while a meteorological station (N20; Fig. 1a) provided wind velocity measurements throughout the experiment period.

b. Methods

1) General methods

All measurements were hourly averaged, and the velocities rotated into the HB06 coordinate system cross-shore u and alongshore v velocities. Hourly estimates of significant wave height (H_s) and (energy weighted) mean period (T_m) were estimated by standard spectral analysis techniques (see Kuik et al. 1988; Herbers et al. 1999) at surfzone frames and the CDIP buoy. The off-diagonal radiation stress term S_{xy}/ρ was estimated from the spectra and directional moments (Kuik et al. 1988) derived from the pressure sensor and ADV data (e.g., Feddersen 2004, 2012). Observed N20 wind velocities (Fig. 1a) were used to estimate the wind stresses using the neutral drag law of Large and Pond (1981) after correcting for the elevation of the wind sensor above the sea surface and accounting for the influence of waves (Large et al. 1995). Observed and modeled subtidal velocities and temperatures (denoted by subscript ST) are estimated by low-pass filtering using a PL64 filter (Limeburner et al. 1985) with a 33^{-1} cph half-amplitude cutoff.

2) Empirical orthogonal functional analysis

Empirical orthogonal function (EOF) analysis is used to identify the dominant vertical or cross-shore structure of velocity and temperature fluctuations. At a mooring location, EOF analysis separates the vertical $[\phi^{(n)}(z)]$ and temporal $[A^{(n)}(t)]$ variability into orthogonal modes such that

$$F_{\mathrm{ST}}(z,t) = \sum_{n=1}^{N} A^{(n)}(t)\phi^{(n)}(z), \tag{1}$$

where F_{ST} is either subtidal velocity or temperature, N is the total number of vertical measurement elevations, and the $n = 1$ mode has the most variance. Similarly, at a particular water depth (e.g., $z = 0$), EOF analysis separates the cross-shore $[\psi^{(n)}(x)]$ and temporal $[B^{(n)}(t)]$ variability into orthogonal modes, that is,

$$F_{\mathrm{ST}}(x, z = 0, t) = \sum_{n=1}^{N} B^{(n)}(t)\psi^{(n)}(x), \tag{2}$$

where N is the total number of moorings in a cross-shore transect (see Fig. 1b). Complex EOF (cEOF) analysis (Kundu and Allen 1976) is used on the complex velocity field ($w = u + \mathrm{i}v$, where $\mathrm{i} = \sqrt{-1}$), and thus the cEOF spatial and temporal modes are complex. The time mean of velocity and temperature signal (section 5a) are removed prior to cEOF analysis.

3) Model data comparison statistics

Model data comparison is quantified through three metrics: bias, root-mean-square error (RMSE), and the square of the Pearson correlation coefficient (r^2). Bias is estimated as

$$\mathrm{Bias} = \langle M(t) - O(t) \rangle, \tag{3}$$

where O and M represent observed and modeled quantity, respectively, and $\langle\ \rangle$ is the time average. The RMSE is calculated as

$$\mathrm{RMSE} = \langle [M(t) - O(t)]^2 \rangle^{1/2}. \tag{4}$$

3. Model description, grid setup, and forcing

a. Model description

The open-source COAWST modeling system (Warner et al. 2010) couples an atmospheric [Weather Research and Forecasting (WRF) model], wave (SWAN), three-dimensional (3D) circulation and stratification (ROMS) and sediment transport models. The coupled modeling system has been validated in a variety of applications including the study of wave–current interaction and depth-varying cross- (e.g., undertow) and alongshore currents in the surfzone (Kumar et al. 2011, 2012) and a tidal inlet (Olabarrieta et al. 2011), atmospheric–ocean–wave interactions under hurricane forcing (Olabarrieta et al. 2012), and sediment dispersal in shallow semi-enclosed basins (Sclavo et al. 2013). Here, COAWST is used in a coupled ROMS and SWAN mode.

The third generation, spectral SWAN wave model (Booij et al. 1999; Ris et al. 1999) includes shoaling, wave refraction due to both bathymetry and mean currents, energy input due to winds, energy loss due to white-capping, bottom friction, and depth-limited breaking. SWAN inputs include a bathymetric grid, incident wave spectra boundary conditions, wind to allow wind-wave generation, and mean velocity for current-induced wave refraction. The model outputs directional wave spectra from which significant wave height H_s, mean wave period T_m, and radiation stress (e.g., S_{xy}/ρ) can be calculated.

ROMS is a three-dimensional, free-surface, bathymetry following numerical model–solving finite-difference approximation of Reynolds-averaged Navier–Stokes (RANS) equations with the hydrostatic and Boussinesq approximations (Shchepetkin and McWilliams 2005; Haidvogel et al. 2008; Shchepetkin and McWilliams 2009). The COAWST wave–current interaction algorithm is based on the vortex force formalism (Craik and Leibovich 1976), separating conservative (McWilliams et al. 2004) and non-conservative (depth-limited breaking-induced acceleration) wave-induced effects (Uchiyama et al. 2010; Kumar et al. 2012). ROMS and SWAN are two-way coupled (Warner et al. 2008b,a), allowing vertically sheared currents (Kirby and Chen 1989) to modify the wave field.

b. U14 model grids and forcing

Here, COAWST is set up as a one-way child grid to the grid system used by U14, providing initial and boundary conditions. The U14 grid system consists of quadruply nested model domains with an offline, one-way nesting technique (see Mason et al. 2010; U14). The U14 grids downscale from a domain of the U.S. West Coast and eastern Pacific (L0, resolution $\Delta = 5$ km, area 4000×3000 km^2), to the Southern California Bight (L1, $\Delta = 1$ km, area 800×700 km^2), to the interior bight region (L2, $\Delta = 250$ m, area 500×300 km^2; Fig. 2a), to the San Pedro Bay (L3, $\Delta = 75$ m, area 80×70 km^2; Fig. 2b). The model bathymetries are from the 30-arc-s global bathymetry [Shuttle Radar Topography Mission 30 arc s dataset (SRTM30); Becker et al. 2009], with refinement using the 3 s (~90 m) NOAA–NGDC coastal relief dataset for the nearshore regions. These domains have 40 (L0, L1, and L2) or 32 (L3) bathymetry-following vertical levels.

The outermost U14 domain (L0) is forced with a combination of lateral boundary conditions from an assimilated global oceanic dataset (Carton and Giese 2008), relaxing to monthly averaged sea surface temperature and salinity, and includes freshwater flux from river runoff. A doubly nested WRF model with $\Delta = 18$ km and $\Delta = 6$ km, embedded within the NCEP North American Regional Reanalysis, provides surface wind stress, heat, and radiative and freshwater (evaporation–precipitation) flux boundary conditions to the parent (L0, $\Delta = 18$ km) and all the child grids ($\Delta = 6$ km). The model grid is spun for 15 yr with climatological surface forcing, prior to the 1 August 2006 experiment commencement.

Daily L0 solutions are used as a lateral boundary condition for L1. In addition, barotropic tidal elevation and velocities of M_2, S_2, N_2, K_2, O_1, P_1, Q_1, M_f, and M_m are projected onto the lateral boundaries of L1 with amplitude and phases obtained from the TOPEX/Poseidon (TPXO7.1) global tidal prediction model (Egbert et al. 1994). The L1 solutions are used as L2 lateral boundary conditions, and L2 solutions provide L3 boundary conditions, both every 2 h.

c. HB06 model grids, setup, boundary conditions, and forcing

The U14 L3 grid provides boundary conditions for the HB06 L4 grid ($\Delta = 50$ m) that has a 15-km cross-shore and 30-km alongshore region in the San Pedro Bay offshore of Huntington and Newport Beach, California, that spans the shelf break to inner shelf and surfzone (Fig. 2c). The L4 grid provides information to the innermost L5 grid ($\Delta = 10$ m) that spans approximately 6 km alongshore and cross shore (Fig. 2d), which encompasses the midshelf to the surfzone, where the HB06 instrumentation was located (Fig. 1). L4 and L5 have 20 bathymetry-following levels, with bathymetry $h(x, y)$ from the NOAA tsunami DEM (Caldwell et al. 2011). Biweekly bathymetry surveys from 7 September to 10 October, spanning ±500 m from the instrument transect, demonstrated surfzone bathymetric evolution (e.g., Clark et al. 2011). However, lack of coverage in the substantial part of L5 and the requirement for alongshore consistency does not allow for the use of observed bathymetry in model simulations.

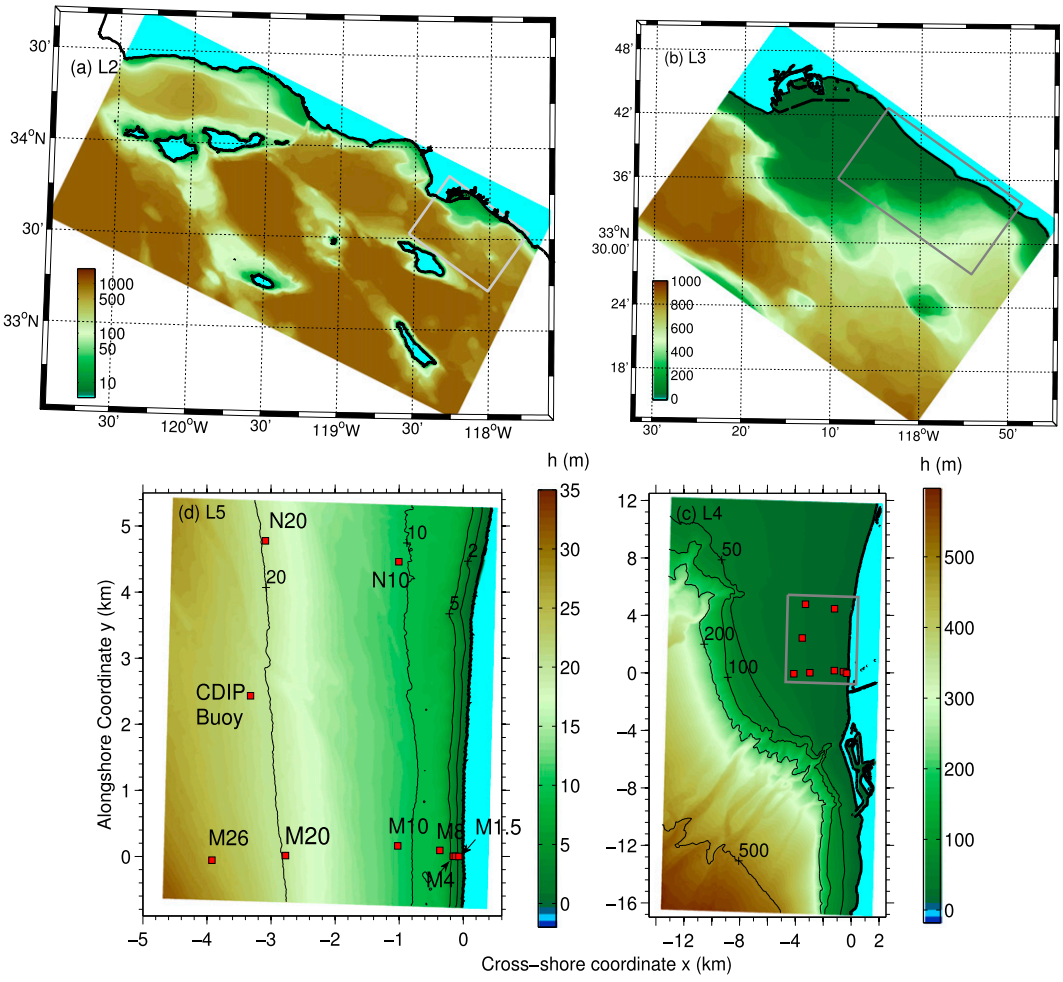

FIG. 2. Model grids showing (a) interior shallower area of the SCB, (b) the SPB, (c) outer shelf to inner shelf and (d) midshelf to surfzone region adjacent to Huntington and Newport Beach in the SPB. The color shading represents the bathymetry, while red squares show the location of offshore moorings, CDIP wave buoy, and an array of surfzone frames, respectively. These grids have a resolution of 250 (L2), 75 (L3), 50 (L4), and 10 m (L5), respectively. Note that the water depth h is shown as a positive number in these figures.

The model simulations for both the L4 and L5 grids were conducted for 92 days (from 1 August to 1 November 2006) with a ROMS baroclinic time step of 8 and 4 s, respectively; the wave action density in SWAN evolves with a time step of 120 s and 60 s, respectively; and the exchange of information between the circulation and wave models occurred every 360 s.

ROMS bottom stress is determined using a logarithmic layer drag with a roughness length of $z_0 = 0.001$ m, and a $k-\epsilon$ turbulence closure model is used to close the momentum balance equation. More complex bottom stress algorithms that include wave effects do not result in substantial improvement in 10–20-m water depths (Ganju et al. 2011). However, neglecting wave effects in the shallow waters of the surfzone and inner shelf may result in underestimated bottom stress (e.g., Feddersen et al. 2000). A horizontal eddy viscosity of $0.1\,\mathrm{m^2\,s^{-1}}$ is used. The SWAN wave action balance equation is solved in frequency and directional space with 48 frequencies between 0.01 and 1 Hz and 60 directional bands with a directional width of 6° spanning 360°. The parameter $\gamma = 0.5$ (ratio of wave height to water depth at which wave breaking occurs) is used to simulate inception of depth-limited wave breaking.

The SWAN L4 grid lateral boundary wave forcing is a frequency–directional wave spectra time series derived from regional, deep-water, CDIP wave buoy spectra estimates farther offshore that were transformed to the boundary with ray-based spectral refraction methods (O'Reilly and Guza 1991, 1993). The wave fields determined for L4 are subsequently used to provide spectral estimates of wave forcing for L5. Wind-wave generation

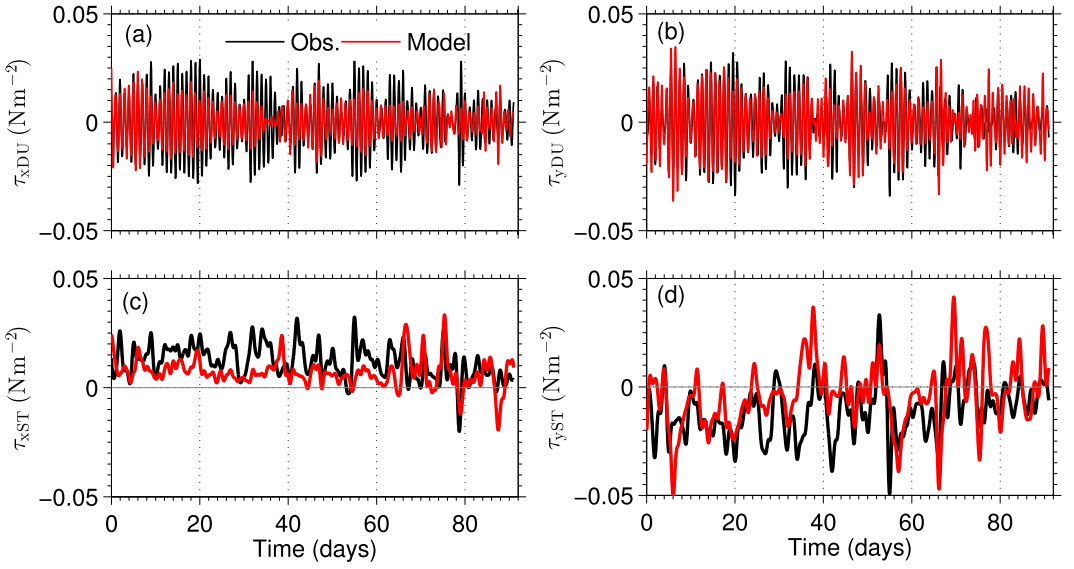

FIG. 3. Observed (black) and modeled (red) wind stress at N20 (Fig. 1) vs time in the (top) diurnal (16^{-1} to 33^{-1} cph) and (bottom) subtidal ($<33^{-1}$ cph) frequency bands and for (left) cross-shore (τ_x) and (right) alongshore (τ_y) components. Time corresponds to days from 1 Aug 2006 (UTC).

within L4 and L5 is negligible. The ROMS L4 and L5 lateral open boundary conditions are inherited from L3 and L4, respectively. A Chapman boundary condition (Chapman 1985) assuming the signal leaves at the shallow-water speed, together with a Flather boundary condition (Flather 1976), radiates out barotropic (depth averaged) normal flows and sea surface elevation. A Chapman boundary condition is used for tangential barotropic velocities. The standard Orlanski radiation boundary condition (Raymond and Kuo 1984) is used for baroclinic (three dimensional) normal and tangential velocities. Temperature and salinity fields and baroclinic velocities are strongly nudged (Marchesiello et al. 2001; Mason et al. 2010) to incoming flow (ΔT = 30 min) and weakly nudged to outgoing flows (ΔT = 365 days) of the outer parent grid.

d. Model and observed winds

Accurate wind forcing is critical for SCB inner-shelf circulation modeling (Lentz and Winant 1986). The SCB has complex coastline shape and local islands, leading to significant wind variability at length scales from the SCB to <10 km (e.g., Winant and Dorman 1997; Conil and Hall 2006). The wind field used by ROMS in domains L4 and L5 must be consistent with the winds used in the L0–L3 nested domains that provide ocean currents and temperature boundary conditions to L4. Thus, the WRF model wind stress, which forces L0–L3, also forces L4 and L5, and observed winds are not used.

The WRF model has been extensively used to simulate wind stress in the eastern Pacific region and, in general, favorably compares against observations on seasonal and monthly scales (e.g., Boé et al. 2011) and daily mean wind speeds (e.g., Huang et al. 2013; Capps et al. 2014). However, validation near the land–sea boundary such as the HB06 region is limited. WRF-simulated hourly wind stresses τ are evaluated against those estimated using wind velocities measured at N20 (see Fig. 1a). Modeled and observed wind stresses are bandpass filtered at subtidal (denoted with the subscript ST; $<33^{-1}$ cph) and diurnal (denoted with the subscript DU; 16^{-1} to 33^{-1} cph) frequency bands. Wind stress contribution is negligible at higher frequencies ($>16^{-1}$ cph). Superscripts m and o denote modeled and observed quantities, respectively.

Observed cross-shore and alongshore diurnal wind stresses $\tau^{(o)}_{x\mathrm{DU}}$ and $\tau^{(o)}_{y\mathrm{DU}}$ (Figs. 3a,b) vary from −0.03 to 0.03 N m^2 and have similar standard deviation (σ = 0.01 N m^2). Modeled cross-shore (Fig. 3a) and alongshore (Fig. 3b) diurnal wind stresses $\tau^{(m)}_{x\mathrm{DU}}$ and $\tau^{(m)}_{y\mathrm{DU}}$ are strongly correlated to those observed (r^2 = 0.68, 0.65, respectively) with negligible bias. Model to data best-fit slopes for diurnal cross-shore and alongshore wind stresses are 0.53(±0.03) and 0.77(±0.05), respectively, suggesting underestimation of diurnal wind stress magnitude.

Observed subtidal cross-shore (Figs. 3c) and alongshore (Fig. 3d) wind stresses $\tau^{(o)}_{x\mathrm{ST}}$ and $\tau^{(o)}_{y\mathrm{ST}}$ vary from −0.04 to 0.05 N m^2 Modeled and observed subtidal cross-shore wind stresses are directed positive (i.e., onshore Fig. 3c). However, $\tau^{(m)}_{x\mathrm{ST}}$ are only weakly correlated (r^2 = 0.07) to observations, with a small positive bias (0.005 N m^2) and a best-fit slope of 0.47(±0.04). The

alongshore subtidal wind stress $\tau_{y\mathrm{ST}}^{(o)}$ standard deviation is twice that of cross-shore $\tau_{x\mathrm{ST}}^{(o)}$. Subtidal alongshore wind stress $\tau_{y\mathrm{ST}}^{(m)}$ oscillates with a time scale of 5 to 10 days (Fig. 3d). Observed and modeled alongshore subtidal wind stresses are moderately correlated ($r^2 = 0.24$), albeit with a bias of $-0.007\,\mathrm{N\,m^2}$ and slope of $0.47(\pm 0.06)$.

Differences in observed and modeled wind stress may occur because of WRF's coarse resolution (i.e., $\Delta = 6\,\mathrm{km}$) and down-scaling effects (from a larger grid) at the land–sea transition. In addition, uncertainties in observed wind stress estimation due to instrument or methodology errors may account for some differences in best-fit slopes, although likely not the correlations. As WRF winds must be used in L4 and L5 to maintain consistency with the offshore nested domains, differences in observed and modeled wind stress will lead to different model and observed subtidal circulation, in part motivating the statistical model data comparison (section 5).

4. Results: Direct model data comparison

The SPB midshelf to surfzone circulation dynamics are complex because of the interaction of coastally trapped waves (e.g., Hickey 1992), meso- and submesoscale eddies (e.g., Dong et al. 2009), wind (e.g., Lentz and Winant 1986), tidal, and wave breaking–induced forcing (Feddersen 2012). Here, the coupled ROMS–SWAN model performance is quantified from the midshelf to the surfzone by directly comparing model (from L5 grid; Fig. 2d) and observed time series of tidal, wave, and circulation parameters at different mooring locations.

a. Model data comparison of tidal elevation at M8

Model tidal forcing (sea surface elevation and barotropic velocities) is provided at the open lateral boundaries of grid L1 (see U14), approximately 800 km offshore from the HB06 region. Model barotropic tides subsequently propagate through the one-way nested grid system (Fig. 2) modified by model bathymetry, generating internal tides and tidal residual flows (e.g., Geyer and Signell 1990). The SCB has complicated bathymetry with variable coastline, islands, and ledges. There are only a limited number of model evaluation studies focused on barotropic tidal propagation in the SCB (Buijsman et al. 2012). In the surfzone, tides modulate the water depth, changing the cross-shore location of wave breaking and thereby also the location and strength of surfzone currents (Thornton and Kim 1993). Thus, modeling exchange between the midshelf to the surfzone requires accurate simulation of barotropic tides.

Model data comparison of tides is performed by comparing amplitude of the dominant tidal constituents (O_1, K_1, N_2, M_2, and S_2) at M8 through harmonic analysis (T_TIDE package; Pawlowicz et al. 2002). Model diurnal tidal constituents (O_1 and K_1) have relatively small-amplitude error of <10% (Fig. 4), while semidiurnal tidal constituent (N_2, M_2, and S_2) amplitudes are underestimated by $\approx 1/3$ (Fig. 4). The more accurate simulation of diurnal relative to semidiurnal tidal constituents is consistent with the results of Buijsman et al. (2012) at other tidal stations in the SCB; however, the semidiurnal constituent underprediction is larger here. Maximum phase difference in modeled and observed tidal constituents is less than an hour. This indicates that with specified offshore tidal L1 boundary conditions, the model tidal propagation through the multiply nested 800-km-long domains with variable bathymetry and no tidal body force is largely well simulated. Prescription of barotropic tidal boundary conditions (sea surface elevation and barotropic tidal velocities) at L4 and L5 domains would reduce the error in barotropic tidal elevation and flows. However, this approach creates inconsistent baroclinic velocity and temperature boundary conditions at L4, preventing mesoscale, submesoscale, and internal tide features from entering the domain, which are important in the shelf and surfzone regions (e.g., Nam and Send 2011; Suanda et al. 2014; Sinnett and Feddersen 2014).

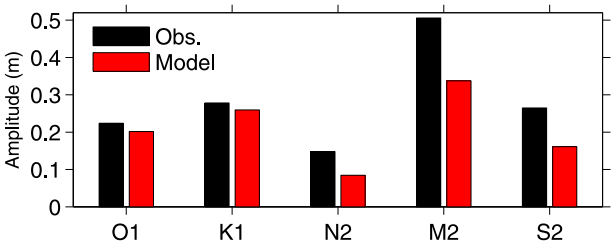

FIG. 4. Observed (black) and modeled (red) amplitude for tidal constituents O_1, K_1, N_2, M_2, and S_2 at M8.

b. Model data comparison of wave statistics at M4

Accurate model wave forcing is required for realistic simulation of surfzone circulation, alongshore tracer transport, and exchange between the surfzone and the inner shelf. Modeled and observed significant wave height H_s, mean wave period T_m, and radiation stress S_{xy}/ρ (where ρ is the water density) are compared at M4 (see Fig. 1c) outside the surfzone ($x = -160\,\mathrm{m}$) in ≈4-m water depth (Fig. 5). All wave properties are estimated over the 0.05–0.25-Hz frequency band.

Observed M4 $H_s^{(o)}$ varied from 0.5 to 1.25 m generally on subtidal time scales (Fig. 5a). Observed and modeled H_s are very similar with small RMSE = 0.08 m. The observed mean wave period $T_m^{(o)}$ varied from 8 to 12 s (Fig. 5b), which is favorably modeled $T_m^{(m)}$ with RMSE = 0.9 s.

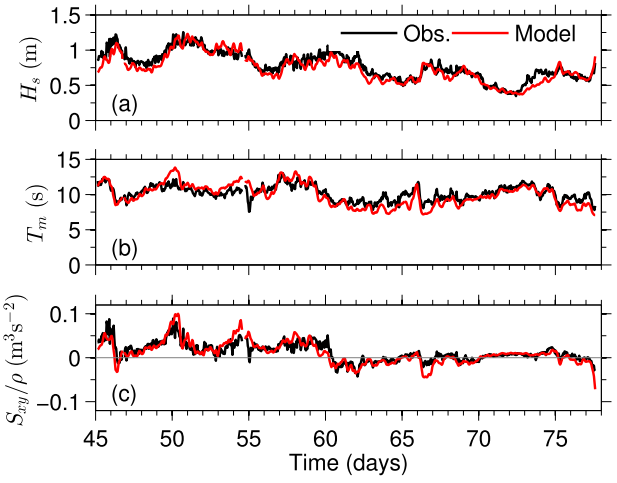

FIG. 5. Observed (black) and modeled (red) (a) significant wave height H_s, (b) mean wave period T_m, and (c) radiation stress component S_{xy}/ρ vs time at M4 (Fig. 1). Time corresponds to days from 1 Aug 2006 (UTC).

Here, the coupled ROMS–SWAN model wave forcing, which depends upon wave dissipation (e.g., Battjes and Janssen 1978; Thornton and Guza 1983), drives surfzone circulation with the vortex force formalism (e.g., McWilliams et al. 2004; Uchiyama et al. 2010; Kumar et al. 2012). Cross-surfzone integrated, this forcing is equivalent to the incident radiation stress term S_{xy}/ρ, shown to drive surfzone alongshore currents and dominate the surfzone alongshore momentum balance (e.g., Longuet-Higgins 1970; Feddersen et al. 1998; Ruessink et al. 2001). At M4, seaward of the surf zone, the model S_{xy}/ρ reproduces the observations with small negative bias and RMSE = 0.03 m^3 s^{-2}. The model captures the day 61 S_{xy}/ρ sign change, which is important for the correct surfzone alongshore currents' sign. The model accurately simulates the waves seaward of the surfzone (Fig. 5) due to the accurate, CDIP, wave buoy–derived wave boundary conditions. Similarly, accurate wave model performance is also found (not shown) at the CDIP wave buoy in 22-m water depth (see Fig. 1a).

c. *Model data comparison of waves and currents in the nearshore (M3 and M1.5)*

Wave variability in the nearshore and associated generation of undertow and alongshore and cross-shore currents induce tracer alongshore transport and cross-shore exchange. Model data comparison of hourly averaged waves and currents is performed at nearshore sites M3 (just seaward of the surfzone, at mean h = 3.2 m) and M1.5 (within the surfzone at mean h = 1.4 m; see Fig. 1). This region's currents are strongly affected by the breaking of surface gravity waves. At M1.5 and M3, modeled currents are taken at the mean ADV sample volume vertical location above the bed, 0.8 and 0.4 m for M3 and M1.5, respectively. Note that as surfzone bathymetry evolved and was different than the fixed DEM bathymetry (e.g., Fig. 1), the cross-shore x location of M1.5 is shifted 20 m onshore (Table 1) so that the model data comparison is performed in the same mean h.

Seaward of the surfzone at M3, $H_s^{(o)}$ varies from 0.5 to 1.3 m, with larger waves from days 45–60, with weak tidal modulation (Fig. 6a). As with the detailed results at M4 (Fig. 5), $H_s^{(m)}$ compares favorably to the observations with small RMSE = 0.08 m. At M1.5, both $H_s^{(o)}$ and $H_s^{(m)}$ are tidally modulated (Fig. 6b) because of the stronger depth-limited breaking at lower tides. Setup induced by cross-shelf winds is negligible. The modeled $H_s^{(m)}$ reproduces the observed variability, nevertheless, $H_s^{(o)}$ tidal modulation is stronger than $H_s^{(m)}$ because of the tidal amplitude errors (see Fig. 4). The relatively small errors (RMSE = 0.09 m) indicate that surfzone breaking wave energy dissipation is well represented by the SWAN algorithm (Battjes and Janssen 1978), as previously shown for other coasts (Ruessink et al. 2001).

At M3, the observed alongshore current $v^{(o)}$ varies between ± 0.3 m s^{-1} (Fig. 6c), with generally positive (northwestward) current from days 45–60 and negative current from days 60–70. The modeled $v^{(m)}$ is similar to $v^{(o)}$ with RMSE = 0.12 m s^{-1}. At M1.5, $v^{(o)}$ varies from ± 0.6 m s^{-1} (Fig. 6d) with strong tidal oscillations due to tidally induced depth-limited wave breaking when M1.5 alternates from within to seaward of the surfzone. Consistent with surfzone momentum balances (Feddersen 2012), the observed and modeled v sign follow the incident observed and modeled S_{xy}/ρ (Fig. 5c). Relatively, higher bias (-0.16 m s^{-1}) and RMSE (0.21 m s^{-1}) is found for M1.5 $v^{(m)}$. The M1.5 v RMSE is similar to surfzone v RMSE at two other beaches (U.S. East Coast and the Netherlands) using a simple one-dimensional alongshore current model (Ruessink et al. 2001), although these studies used accurate bathymetry and observed incident waves.

At M3, the ADV, observed, cross-shore current $u^{(o)}$ is generally offshore directed (negative), varying from 0 to 0.1 m s^{-1} (Fig. 6e), which the model roughly captures with RMSE = 0.04 m s^{-1}. At M1.5, $u^{(o)}$ is mostly directed offshore varying between 0 and 0.3 m s^{-1} (Fig. 6f) as part of the undertow (e.g., Garcez Faria et al. 2000). Modeled $u^{(m)}$ has RMSE = 0.07 m s^{-1} with tidal oscillation similar to $u^{(o)}$ (Fig. 6f) except for days 57–60, when $u^{(o)}$ is predominantly offshore directed because of a $\pm$20-cm bed accretion/erosion event not accounted for in the model bathymetry. In addition, reproduction of high-frequency

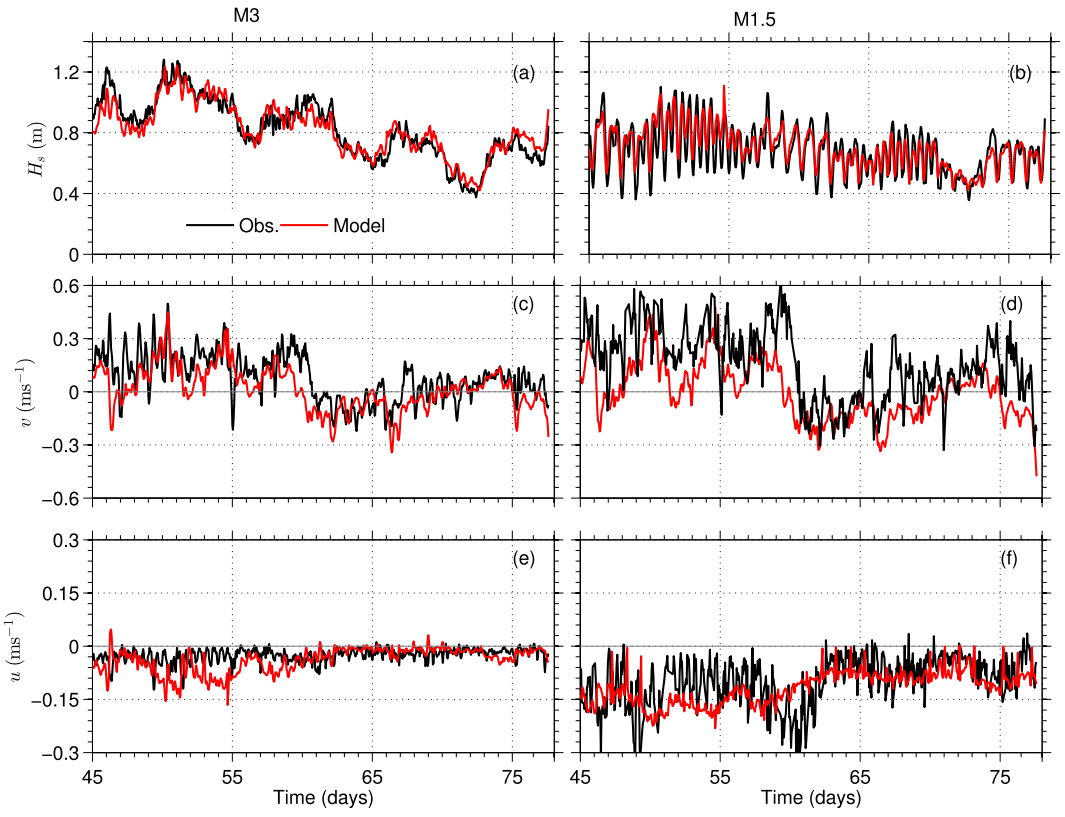

FIG. 6. Observed (black) and modeled (red) hourly averaged (a),(b) significant wave height H_s, (c),(d) alongshore current v, and (e),(f) cross-shore current u vs time at (left) just seaward of the surfzone M3 and (right) surfzone M1.5. In (c)–(f), model currents are at the average height above the bed of the ADVs. Time corresponds to days from 1 Aug 2006 (UTC).

($>10^{-1}$ cph) variability in observed flows is not expected in the absence of unknown high-frequency forcing (e.g., infragravity waves), lack of finer grid resolution, and lack of nonhydrostatic dynamics that influences high-frequency internal waves.

The model has substantial capability in simulating wave heights and alongshore currents in the nearshore and surfzone at a particular mean water depth (Fig. 6), even though the cross-shore bathymetry profile is inaccurate. The model capability in simulating cross-shore currents at a particular height above the bed is reduced as u depends more on dynamical terms that have cross-shore gradients (Kumar et al. 2012). Nevertheless, with accurate bathymetry, the vertical profile of surfzone currents is simulated well with a wave-driven ROMS model (Uchiyama et al. 2010; Kumar et al. 2012). Given the differences in the model and observed cross-shore bathymetry profiles (section 2a), the fact that the modeled v and u are reasonably consistent with the observed indicates that the model (without tuning) accurately simulates the dynamics of surfzone currents.

d. *Model data comparison of subtidal velocity and temperature in midshelf (M26) and inner shelf (M8)*

In the inner and midshelf of the SCB, wind forcing contributes to the subtidal along-shelf current dynamics (e.g., Lentz and Winant 1986). The modeled subtidal wind stress is not correlated with the observed (see section 3d). In addition, subtidal hydrodynamics are also influenced by large-scale pressure gradients (e.g., Hickey et al. 2003) and intrinsic variability manifested in the form of meso- and submesoscale eddies (e.g., Hickey 1992; Dong et al. 2009). Therefore, in a nondata-assimilated model simulation (as conducted here), modeled currents and temperature are not expected to be coherent with the observations. Nevertheless, a model data comparison of temporal and vertical structure of along-shelf current and temperature at the midshelf M26 and inner-shelf M8 moorings (see Fig. 1) is performed in the subtidal band to diagnose differences in vertical structure and temporal evolution.

At M26, the observed along-shelf current $v_{\mathrm{ST}}^{(o)}$ oscillates $\pm 0.3\,\mathrm{m\,s^{-1}}$ on time scales of 5–10 days (Fig. 7a).

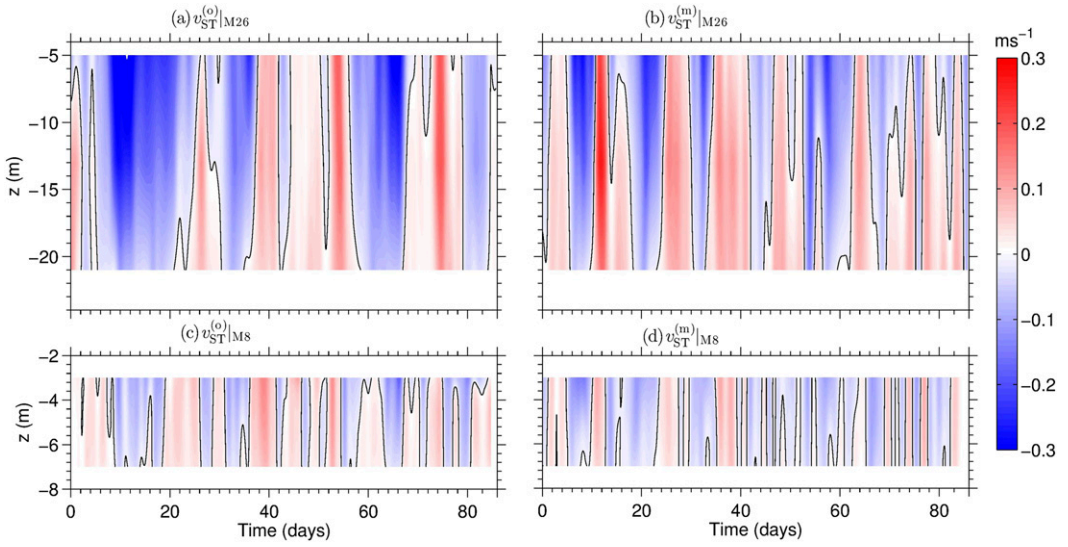

FIG. 7. (left) Observed and (right) modeled subtidal alongshore velocity v_{ST} as a function of z and time at (top) M26 and (bottom) M8. The solid black lines denote zero v. Time corresponds to days from 1 Aug 2006 (UTC).

Modeled alongshore flows $v_{ST}^{(m)}$ (Fig. 7b) are of the same order as $v_{ST}^{(o)}$, although substantial differences occur (e.g., days 10–20 and 50–65). The observed and modeled v_{ST} are unrelated as the observed and modeled depth-averaged (represented with an overbar) subtidal alongshore current $\overline{v}_{ST}$ are uncorrelated ($r^2 < 0.01$). Qualitatively, the observed and modeled vertical structure of v_{ST} are similar. In the inner shelf (M8), observed alongshore current $v_{ST}^{(o)}$ is weaker ($\pm 0.15\,\mathrm{m\,s^{-1}}$) relative to M26 (Fig. 7c), with currents oscillating on time scales of 2–5 days. In general, the modeled alongshore current $v_{ST}^{(m)}$ has similar variability ($\pm 0.15\,\mathrm{m\,s^{-1}}$) and vertical structure as $v_{ST}^{(o)}$ (Fig. 7d). However, the modeled and observed depth-averaged alongshore currents $\overline{v}_{ST}$ are also weakly correlated ($r^2 \approx 0.1$).

The midshelf M26 subtidal temperature $T_{ST}^{(o)}$ varies from 12° to 22°C over a 5–10-day time scale (Fig. 8a). The stratification can be significant with surface to near-bed temperature differences of up to 6°C. The modeled subtidal temperature profile $T_{ST}^{(m)}$ (Fig. 8b) is generally warmer than those observed. The modeled temperature bias is small near the surface (0.2°C) and increases at near-bottom locations (2.0°C). As with along-shelf velocity, M26 modeled and observed depth-averaged temperature $\overline{T}_{ST}$ are weakly correlated. At the inner-shelf mooring M8, $T_{ST}^{(o)}$ (Fig. 8c) varies from 15° to 21°C

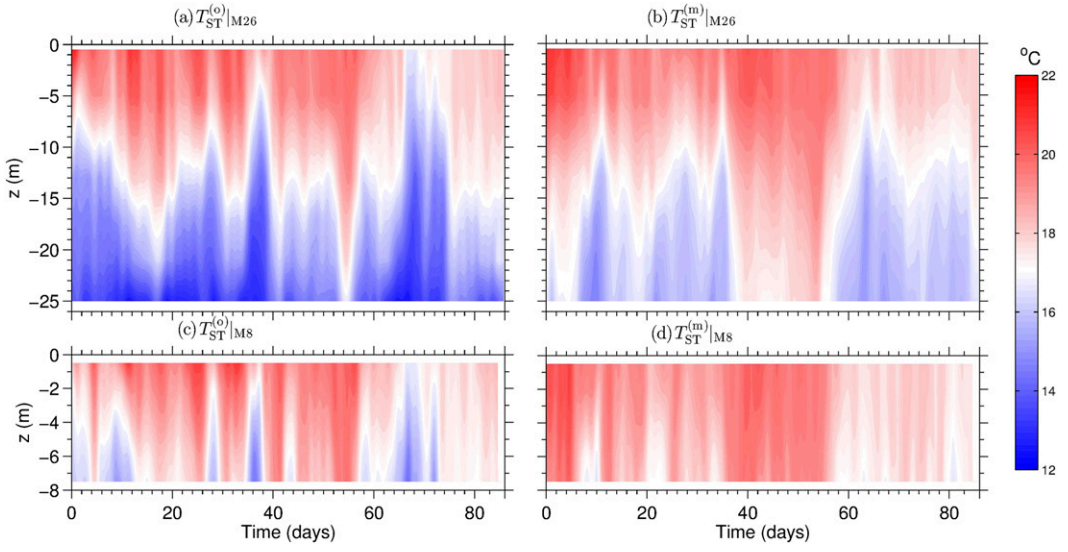

FIG. 8. As in Fig. 7, but for subtidal temperature T_{ST}.

with generally similar stratification as the upper 8 m of M26. Modeled subtidal temperature $T_{ST}^{(m)}$ (Fig. 8d) has similar temporal variability as observed, but also with much weaker stratification. The model $T_{ST}^{(m)}$ near-surface bias is ≈0.1°C, whereas the near-bed bias is stronger ≈1.0°C. At M8, the model and observed T_{ST} temporal variability is unrelated as the depth-averaged temperatures are weakly correlated.

Although observed and modeled currents and temperature have similar temporal variability at mid- and inner-shelf locations (Figs. 7, 8), the model has no predictive capability. Inaccurate modeled variability is due in part to inaccurate wind stresses (Figs. 3c,d). Modeled variability is also set by lateral boundary conditions from the parent grids (Fig. 2), whose errors can be substantial and are not a priori known (McWilliams 2007, 2009). Both forcing and lateral boundary condition errors limit model predictability, motivating the statistical model data comparison presented in section 5.

5. Results: Statistical model data comparison

Here, the model's ability to simulate the temporal variation and vertical structure of velocity and temperature from the mid- to inner shelf is examined by three statistical model data comparisons performed over the duration of each mooring deployment period (Table 1).

a. Vertical structure of mean velocity and temperature

First, a model data comparison is performed on mean velocities and temperatures at the midshelf (M26 and M20) and inner-shelf (M10 and M8) locations (Fig. 9). The mean denoted by $\langle\ \rangle$ is defined over the time data collection occurring at each mooring location (Table 1). At the mid- and inner-shelf mooring locations, the observed mean alongshore current $\langle v^{(o)}\rangle$ is negative (i.e., southeastward) throughout the water column, is ≈0.0 m s^{-1} near bed, and strengthens toward the surface up to −0.1 m s^{-1} (black in Figs. 9a$_1$–e$_1$). At M26–M10, observed mean alongshore current shear $\partial\langle v^{(o)}\rangle/\partial z \approx -0.005\ \mathrm{s}^{-1}$ and is approximately uniform. At M8, the $\partial\langle v^{(o)}\rangle/\partial z$ is weaker than farther offshore (Fig. 9d$_1$). Modeled mean alongshore current $\langle v^{(m)}\rangle$ resembles $\langle v^{(o)}\rangle$ with zero near bed, increasing with z (red in Figs. 9a$_1$–d$_1$). However, at M26–M10, the modeled mean alongshore current shear ($\partial\langle v^{(m)}\rangle/\partial z$) is weaker than observed, resulting in a weaker upper water column $\langle v^{(m)}\rangle$. The observed mean cross-shore current $\langle u^{(o)}\rangle$ is weak (≤0.02 m s^{-1}) in comparison to $\langle v^{(o)}\rangle$ at all depths at all mooring locations (Figs. 9a$_2$–d$_2$), which is reproduced by the model. Mean observed temperature $\langle T^{(o)}\rangle$ profile varies from 14° to 20°C (Figs. 9a$_3$–d$_3$) with an approximately constant mean vertical temperature gradient $\partial\langle T^{(o)}\rangle/\partial z \approx 0.2°\mathrm{C\,m}^{-1}$. Near-surface observed $\langle T^{(o)}\rangle$ and modeled $\langle T^{(m)}\rangle$ are similar at all moorings. However, at depth $\langle T^{(m)}\rangle$ is always warmer than $\langle T^{(o)}\rangle$, which is most pronounced at the midshelf (M26 and M20) locations. The approximately constant modeled vertical mean temperature gradient $\partial\langle T^{(m)}\rangle/\partial z \approx 0.12°\mathrm{C\,m}^{-1}$, about half the observed (except at M10; Fig. 9c$_3$). Modeled and observed stratification and vertical shear differences are further discussed in section 6a.

b. Rotary velocity and temperature spectra

Rotary velocity (u, v) spectra, separating clockwise (CW) and counterclockwise (CCW) motions (Gonella 1972), and temperature spectra are calculated midwater column at midshelf M26, inner-shelf M10, and surfzone M1.5 locations (Fig. 10). The 256-h spectral window (with 50% overlap) provides good spectral stability, although frequency resolution is insufficient to resolve distinct spectral peaks between inertial and diurnal or M_2 and S_2 tidal frequencies. Thus, model and observed spectra are compared in four frequency bands (shaded regions in Fig. 10): subtidal (ST; $<33^{-1}$ cph), diurnal (DU; 33^{-1} to 16^{-1} cph), semidiurnal (SD; 16^{-1} to 10^{-1} cph), and high frequency (HF; $>10^{-1}$ cph).

At the midshelf M26, the ST rotary spectra are red, rapidly decreasing with frequency and are CW and CCW symmetric (black in Fig. 10a$_1$). The M26 temperature spectra are also red in the ST band (black in Fig. 10a$_2$). The DU band rotary and temperature spectra peak (Figs. 10a$_1$,a$_2$) is due to a combination of barotropic tides (for currents), inertial motions, surface heat flux, diurnal barotropic tidal forcing (e.g., Beckenbach and Terrill 2008), and wind forcing (Fig. 4). The larger CW versus CCW diurnal rotary variance suggests sea breeze–forced resonant internal waves that are nonevanescent because of the subtidal vorticity modifying the effective local Coriolis parameter (Lerczak et al. 2001; Nam and Send 2013). In the SD band, the rotary and temperature spectra peak (Figs. 10a$_1$,a$_2$) is at the M_2/S_2 tidal frequency, reflecting barotropic tides (currents) and semidiurnal internal waves. The M26 HF ($>10^{-1}$ cph) rotary and temperature spectra are much weaker than in the other bands and fall off rapidly (Figs. 10a$_1$,a$_2$).

M26 modeled and observed rotary spectra compare favorably in most frequency bands, including the asymmetry in the DU band (red in Fig. 10a$_1$). The CW to CCW ratio of integrated DU band rotary spectral density is similar for the model (3.7) and observed (3.8). The M26 modeled temperature spectra (red in Fig. 10a$_2$) agrees with the observed in the ST band. In DU and SD bands, modeled spectral peaks are at the same frequency as observed but have smaller magnitudes by a factor of 5 (Fig. 10a$_2$), likely because of weaker modeled mean stratification (Fig. 9a$_3$). In the HF band,

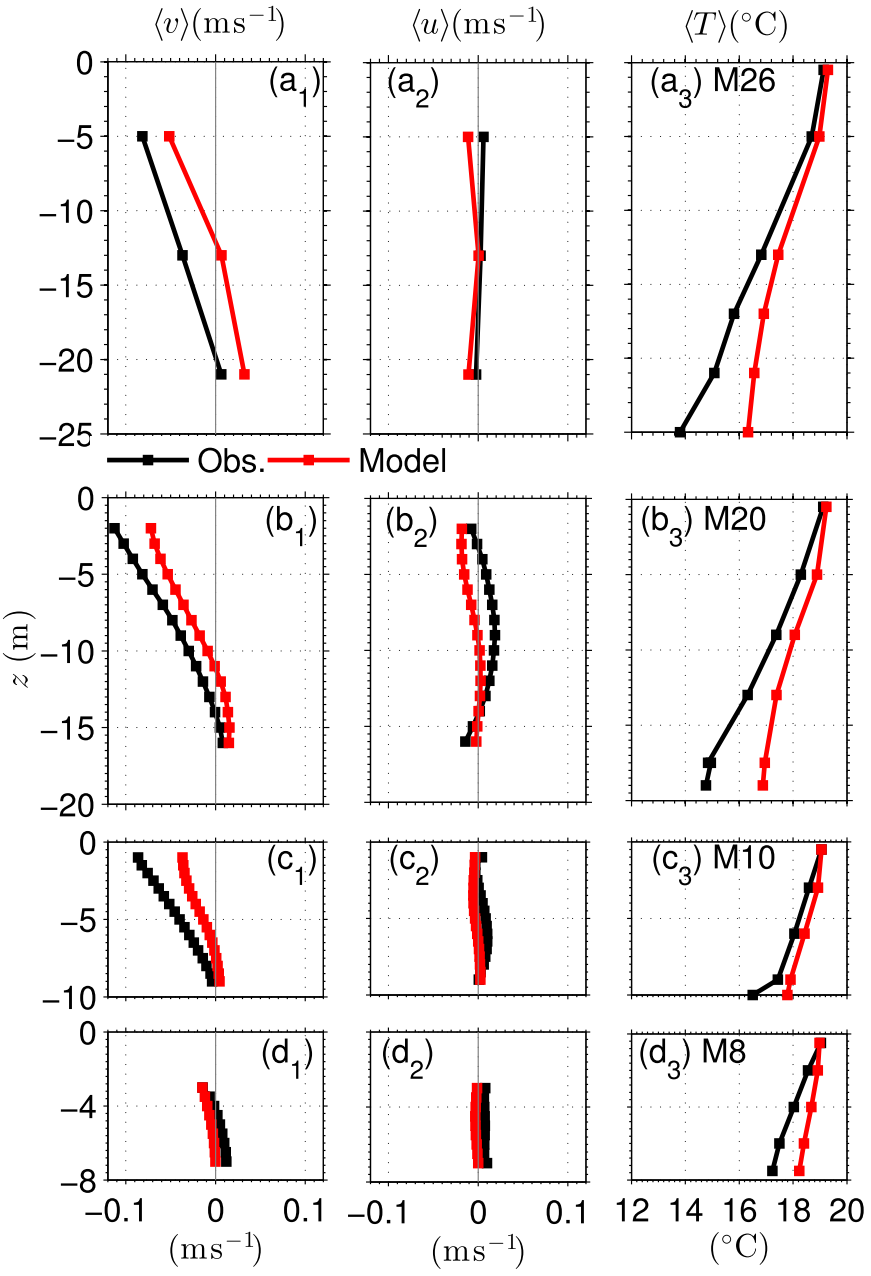

FIG. 9. Vertical profile of mean (left) alongshore velocity $\langle v \rangle$, (middle) cross-shore velocity $\langle u \rangle$, and (right) temperature $\langle T \rangle$ for observed (black) and modeled (red) at (top to bottom) M26, M20, M10, and M8. Note the mean is defined over the time data collection occurred at each mooring (see Table 1).

modeled rotary and temperature spectra are weaker than observed because of the lack of high-frequency surface and boundary forcing but also because of the hydrostatic, approximation-limiting, high-frequency variability.

The inner-shelf M10 observed rotary and temperature (Figs. 10b$_1$,b$_2$) are qualitatively similar to the midshelf M26, with some differences. The M10 observed ST rotary spectra has similar magnitude to M26 but is overall less red with a broader distribution of variance. The M10 DU band rotary spectra are similar in magnitude to M26 but are CW and CCW symmetric probably because of a stronger frictional response in the inner shelf (e.g., Lentz et al. 2001). The SD band rotary spectra are CW and CCW symmetric but slightly smaller than the DU band. In the SD band, the M10 observed temperature spectra is much weaker than at M26. Modeled M10

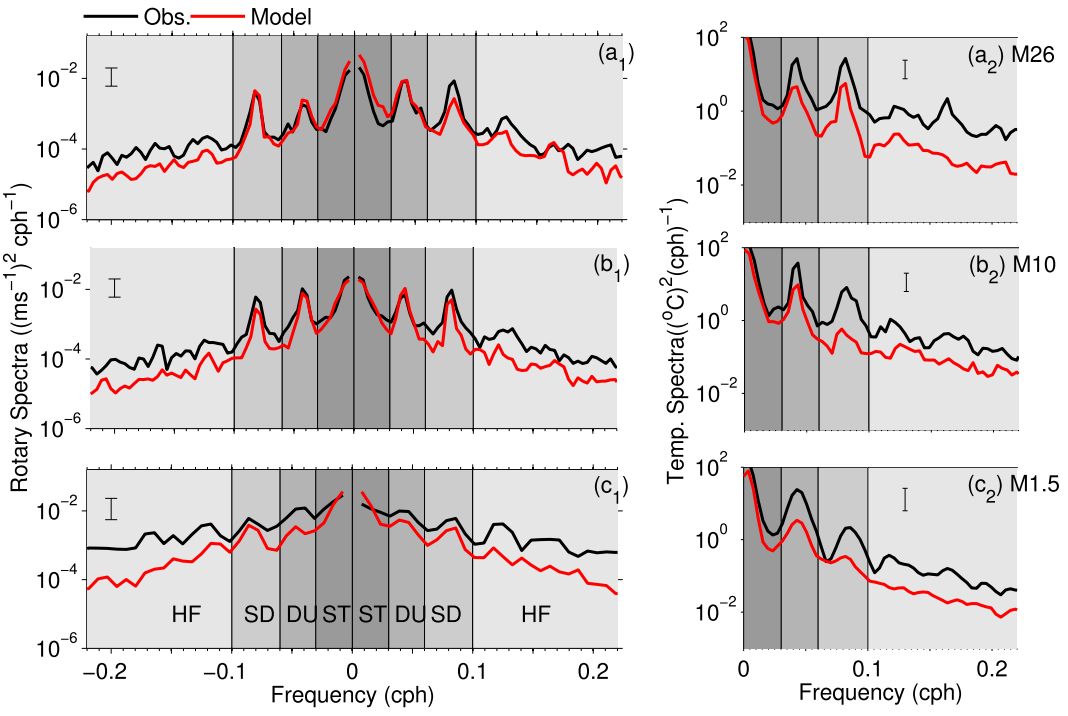

FIG. 10. Observed (black) and modeled (red) middepth (left) velocity rotary spectra and (right) temperature spectra for (from top to bottom) midshelf M26, inner-shelf M10, and surfzone M1.5. The vertical bars represent the 95% confidence interval. For rotary velocity spectra, positive and negative frequencies are clockwise and counterclockwise motions, respectively. The ST ($<33^{-1}$ cph), DU (33^{-1} to 16^{-1} cph), SD (14^{-1} to 10^{-1} cph), and HF ($>10^{-1}$ cph) bands are indicated.

rotary spectra (Fig. 10b$_1$) are similar to that observed in all frequency bands except HF. As at M26, modeled M10 temperature spectra (Figs. 10b$_2$) in the DU, SD, and HF bands are underestimated, with large modeled SD band underestimation.

The surfzone M1.5 observed rotary spectra is whiter, with variance more broadly distributed (Fig. 10c$_1$) than at M26 and M10. The observed ST band variance is nearly flat, the DU band peaks are weak, barely distinguishable from the confidence limits, and the SD band peaks are reduced and broader. The M1.5 observed temperature spectra is qualitatively similar to M10 but with a reduced SD band peak (Fig. 10c$_1$). At M1.5, modeled rotary spectra capture the whitening of the observed and slightly underestimate the observed in all frequency bands. The surfzone M1.5 modeled temperature spectra have a similar pattern to, but underestimates, the variance in the observed temperature spectrum (Fig. 10c$_2$).

c. *EOF analysis of subtidal velocity and temperature*

Given the good ST band spectral model data comparison, observed and modeled dominant vertical modes of subtidal velocities and temperature variability are compared. The temporal variability and vertical structure of subtidal velocities and temperature at moorings M26, M20, M10, and M8 are decomposed into vertical $[\phi^{(i)}(z)]$ and temporal $[A^{(i)}(t)]$ modes by complex (velocity) or standard (temperature) EOF analysis (section 2b). The observed and modeled subtidal velocity is well described by the first cEOF mode $\phi_w^{(1)}(z)$, explaining between 93% and 97% of the variance (Table 2). The first EOF of the observed temperature $[\phi_T^{(1)}]$ explains more variance in shallower than in deeper locations (67% at M26 and 89% at M8; Table 2). The first EOF of modeled temperature has a similar pattern, explaining between 83% (M26) to 94% (M8) of the variance (Table 2).

TABLE 2. Percentage of subtidal velocity and temperature variance explained by the first EOF vertical mode at the indicated mooring site.

	Percent variance explained			
	Velocity		Temperature	
Site	Obs	Model	Obs	Model
M26	93	95	67	83
M20	96	94	74	85
M10	96	95	73	89
M8	95	96	89	93

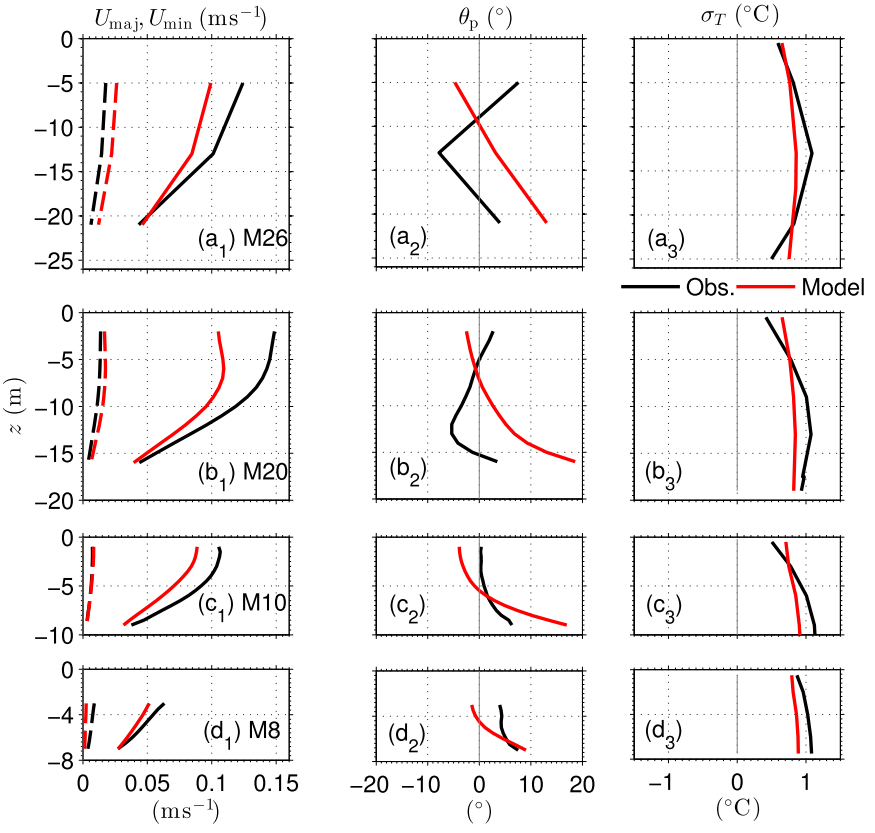

FIG. 11. Vertical (z) profiles of first cEOF, reconstructed, subtidal velocity and temperature variability for observed (black) and modeled (red) at (top to bottom) midshelves M26 and M20 and inner-shelves M10 and M8 sites: (left) the major U_{maj} (solid) and minor U_{min} (dashed) and (middle) principal angle θ_p (relative to $+y$) of the subtidal velocity ellipse. (right) Standard deviation σ_T of reconstructed temperature.

Given the high fraction of variance explained by the first cEOF mode, modeled and observed subtidal cross-shore $u^{(1)}_{ST}(z, t)$ and alongshore $v^{(1)}_{ST}(z, t)$ velocities and temperature $T^{(1)}_{ST}(z, t)$ are reconstructed at each mooring using the first cEOF mode, such that

$$u^{(1)}_{ST}(z,t) = \mathrm{Re}[A^{(1)}_w(t)\phi^{(1)}_w(z)], \quad (5a)$$

$$v^{(1)}_{ST}(z,t) = \mathrm{Im}[A^{(1)}_w(t)\phi^{(1)}_w(z)], \quad \text{and} \quad (5b)$$

$$T^{(1)}_{ST}(z,t) = A^{(1)}_T(t)\phi^{(1)}_T(z), \quad (5c)$$

representing the vertically coherent dominant variability. At each mooring, the reconstructed $u^{(1)}(z, t)$ and $v^{(1)}(z, t)$ are used to estimate subtidal velocity variance ellipse parameters: major $U_{maj}(z)$ and minor $U_{min}(z)$ axes and the principal angle $\theta_p(z)$ with respect to $+y$. These ellipses represent the vertically coherent dominant subtidal motions at each mooring. A θ_p increase with depth ($-z$) represents CCW ellipse veering. Reconstructed temperature $T^{(1)}(z, t)$ standard deviation (std) $\sigma_T(z)$ is also estimated. The ability of the model to statistically reproduce the observations is evaluated by comparing first cEOF derived modeled and observed $U_{maj}(z)$, $U_{min}(z)$, and $\theta_p(z)$ for subtidal velocity and $\sigma_T(z)$ for temperature.

At midshelf (M26 and M20) and inner-shelf (M10 and M8) mooring locations, the observed subtidal flow is strongly polarized with $U^{(o)}_{maj}$ typically $4 \times U^{(o)}_{min}$ (cf. black solid and dashed in Figs. 11a$_1$–d$_1$). The near-bed observed subtidal $U^{(o)}_{maj} \approx 0.03\,\mathrm{m\,s^{-1}}$ increasing to near-surface values of $U^{(o)}_{maj} \approx 0.13\,\mathrm{m\,s^{-1}}$ at M26 and M20 and $U^{(o)}_{maj} \approx 0.07\,\mathrm{m\,s^{-1}}$ at M8. The major axis is always approximately aligned in the alongshore direction [$\theta^{(o)}_p$ is within $\pm 10°$; Figs. 11a$_2$–d$_2$]. At M26 and M20, $\theta^{(o)}_p$ veers $\pm 10°$ CW and CCW in the upper and lower water column, respectively (Figs. 11a$_2$,b$_2$). This $\theta^{(o)}_p$ veering pattern is consistent with surface and bottom Ekman layer dynamics. At M10 and M8, $\theta^{(o)}_p$ veers CCW weakly yet monotonically throughout the water column (Figs. 11c$_2$,d$_2$), indicating bottom boundary layer dominance and the lack of a surface Ekman layer (e.g., Austin and Lentz 2002;

Kirincich and Barth 2009). The small θ_p and CW/CCW veering with depth is consistent with New Jersey inner-shelf observations (Münchow and Chant 2000). At all mooring locations, the subtidal temperature standard deviation $\sigma_T(z)$ varies coherently about $\pm 1°C$ in an approximately vertically uniform manner (Figs. 11c$_3$–d$_d$). At M26 and M20, $\sigma_T^{(o)}$ has a weak maximum in the midwater column (Figs. 11a$_3$–b$_3$), whereas at M10 and M8, $\sigma_T^{(o)}$ is maximum near bed (Figs. 11c$_3$–d$_3$). The $\sigma_T^{(o)}$ structure indicates that the entire water column responds coherently to the delivery of heat.

The model largely reproduces the salient features of the observed subtidal velocity and temperature variability derived from the first cEOF (red in Fig. 11). The modeled subtidal velocity ellipses are similarly polarized [$U_{\text{maj}}^{(m)} \approx 4 \times U_{\text{min}}^{(m)}$] and oriented in the alongshore direction [$\theta_p^{(m)}$ is mostly near 0°]. The modeled near-bed $U_{\text{maj}}^{(m)}$ is similar to the observed $U_{\text{maj}}^{(o)}$. However, the model velocity shear is weaker than observed as $U_{\text{maj}}^{(m)}$ is weaker than $U_{\text{maj}}^{(o)}$ farther up in the water column (Figs. 11a$_1$–d$_1$). At all moorings, $\theta_p^{(m)}$ veers monotonically CCW with depth, indicating bottom boundary layer dominance, in contrast to the observed $\theta_p^{(o)}$ variation at M26 and M20. This may be because of the weaker modeled stratification. The modeled $\sigma_T^{(m)}$ is similar to observed $\sigma_T^{(o)}$ but is more vertically uniform (Figs. 11a$_3$–d$_3$), suggesting uniform response to input heat flux.

6. Discussion

Modeled waves and currents are similar to observation in the surfzone (section 4), and modeled subtidal circulation and temperature variability is statistically similar to the observations (section 5). This motivates further analysis of the observations and model results from the midshelf to the surfzone.

a. *The relationship between stratification and velocity vertical shear*

The model stratification and subtidal velocity vertical shear are weaker than observed (Figs. 8, 9, and 11a$_1$–e$_1$). In a constant stress layer, larger stratification results in an increase in vertical shear (Businger et al. 1971). This pattern is consistent with the larger observed stratification and shear relative to the model. Model compensation of stratification and shear is investigated by examining the ratio of mean stratification to mean squared subtidal vertical shear N^2/S^2. Note that this ratio should not be confused with a gradient Richardson number as the observed and modeled mixing processes that set the mean stratification and subtidal vertical shear occur at shorter time scales that this analysis filters out.

As the first temperature EOF (Figs. 11a$_3$–e$_3$) is largely vertically uniform, the mean stratification $\overline{N}^2$ is estimated solely from the mean temperature profiles (Fig. 9) as

$$\overline{N}^2 = -\frac{g}{\rho_0}\frac{\partial\langle\rho(z)\rangle}{\partial z}, \tag{6}$$

where $\rho_0 = 1025\,\text{kg}\,\text{m}^{-3}$, and $\langle\rho(z)\rangle$ is calculated from $\langle T\rangle$. Salinity effects on density were weak. The subtidal velocity vertical shear S^2 has contributions from both the mean alongshore velocity $\langle v\rangle$ (Figs. 9a$_1$–e$_1$) and from the subtidal variability given by $U_{\text{maj}}(z)$ and $U_{\text{min}}(z)$ (Figs. 11a$_1$–e$_1$). Thus, the mean-squared vertical shear S_{rms}^2 is

$$S_{\text{rms}}^2 = \left(\frac{\partial\langle v\rangle}{\partial z}\right)^2 + \left(\frac{\partial U_{\text{maj}}}{\partial z}\right)^2 + \left(\frac{\partial U_{\text{min}}}{\partial z}\right)^2. \tag{7}$$

Both $\overline{N}^2$ and S_{rms}^2 are estimated over the lower to upper to midwater column, where the velocity shear is relatively uniform (Fig. 11), excluding the near-surface layer. Midshelf (M26 and M20) and inner-shelf (M10 and M8) results are averaged together to give representative mid- and inner-shelf values.

The midshelf observed $\overline{N}^2 \approx 5.3 \times 10^{-4}\,\text{s}^{-2}$ and $S_{\text{rms}}^2 \approx 9.7 \times 10^{-5}\,\text{s}^{-2}$. The modeled midshelf $\overline{N}^2 \approx 3.7 \times 10^{-4}\,\text{s}^{-2}$ and $S_{\text{rms}}^2 \approx 6.9 \times 10^{-5}\,\text{s}^{-2}$ are reduced relative to the observed (consistent with Figs. 9 and 11). This results in similar midshelf observed $\overline{N}^2/S_{\text{rms}}^2 = 5.5$ and modeled $\overline{N}^2/S_{\text{rms}}^2 = 5.4$. In the inner shelf, the observed $\overline{N}^2 \approx 5.1 \times 10^{-4}\,\text{s}^{-2}$ and the shear $S_{\text{rms}}^2 \approx 1.6 \times 10^{-4}\,\text{s}^{-2}$. The inner-shelf modeled $\overline{N}^2 \approx 3.4 \times 10^{-4}\,\text{s}^{-2}$ and $S_{\text{rms}}^2 \approx 1.0 \times 10^{-4}\,\text{s}^{-2}$ are also reduced relative to the observed. This results in similar inner-shelf observed $\overline{N}^2/S_{\text{rms}}^2 = 3.2$ and modeled $\overline{N}^2/S_{\text{rms}}^2 = 3.4$ ratios that are reduced relative to the midshelf.

Continental shelf vertical mixing due to internal waves and bottom boundary layer processes for the subcritical Richardson number has been parameterized where the vertical eddy viscosity $\kappa_{zz} \propto S/N$ (Mackinnon and Gregg 2005). With similar modeled and observed $\overline{N}^2/S_{\text{rms}}^2$ and similar cross-shelf structure from mid- to inner shelf, this suggests that model vertical mixing is representative of the observations and that reduced model stratification $\overline{N}$ (Fig. 9, right column) is not due to model overmixing. Furthermore, this suggests that if the model mean stratification were equal to the observed, then the modeled subtidal velocity shear would also approximately equal the observed. Reasons for the underprediction of model mean stratification are discussed in section 6b.

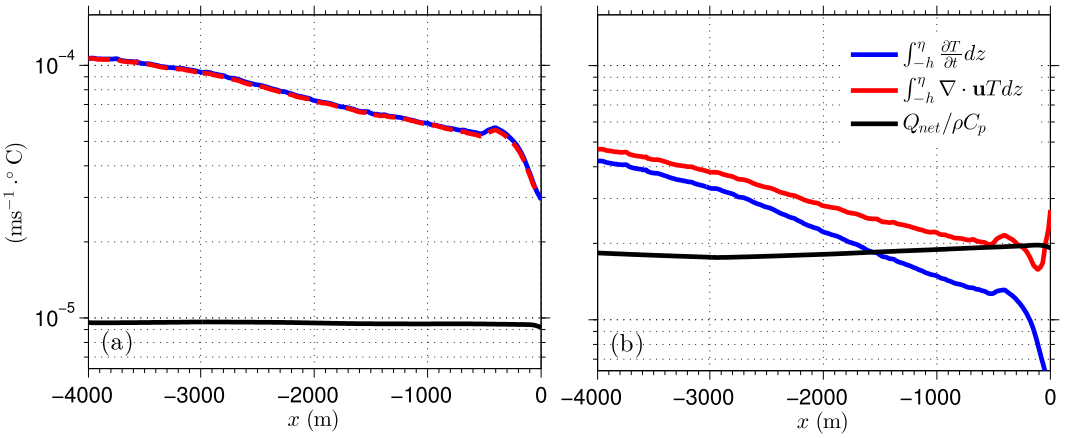

FIG. 12. Root-mean-square of modeled heat budget terms vs cross-shore distance at (a) synoptic ($336^{-1} <$ Freq, $< 33^{-1}$ cph) and (b) fortnightly and longer time scales (Freq. $< 336^{-1}$ cph). Heat content time derivative ($\int_{-h}^{\eta} \partial T/\partial t\, dz$), lateral advective heat flux divergence ($\int_{-h}^{\eta} \nabla_H \cdot \mathbf{u} T\, dz$), and surface heat flux ($Q_{\text{net}}/\rho C_p$) are indicated in the legend.

b. *Model subtidal vertically integrated heat budget*

The relative role of surface and advective heat flux gradients in driving subtidal temperature variability is examined with a model-based subtidal, vertically integrated heat budget where the vertically integrated temperature time derivative is balanced by surface heat fluxes and the lateral advective heat flux divergence, that is,

$$\int_{-h}^{\overline{\eta}} \frac{\partial T}{\partial t} dz = \frac{Q_{\text{net}}}{\rho C_p} - \int_{-h}^{\overline{\eta}} \nabla_H \cdot (\mathbf{u} T)\, dz, \qquad (8)$$

where $\overline{\eta}$ is the mean sea surface elevation, Q_{net} is the net (radiative and air–sea) surface heat flux provided by WRF, C_p is the specific heat capacity of seawater, $\nabla_H \cdot$ is a horizontal divergence, and $\mathbf{u}$ is the model horizontal velocity vector. As with the modeled wind stress, the modeled Q_{net} may have error near the land–sea boundary. However, in the absence of any heat flux measurement, errors in the modeled Q_{net} cannot be quantified. The subtidal component of the three terms in (8) is estimated on the cross-shore instrument transect (Fig. 1). These terms are separated into synoptic ($336^{-1} <$ Freq. $< 33^{-1}$ cph) and fortnightly and longer time scales (Freq. $< 336^{-1}$ cph or >14 days) that include the mean using the PL64 filter (Limeburner et al. 1985) with appropriate half-amplitude cutoff. The cross-shore distribution of root-mean-square heat budget terms [(8)] in the synoptic and fortnightly bands is shown in Fig. 12.

At synoptic time scales, the modeled vertically integrated temperature time derivative ($\int_{-h}^{\overline{\eta}} \partial T/\partial t\, dz$) and advective heat flux divergences essentially balance at all cross-shelf locations from the midshelf to the surfzone (blue and red lines, Fig. 12a). The modeled surface heat flux term (black line, Fig. 12a) is 8× smaller on the midshelf ($x < -2500$ m) and 3× smaller in the surfzone ($x > -160$ m) than the other two terms, indicating that temperature variability is not principally due to surface heat flux. Similar balances on synoptic time scales have been observed in the SCB (e.g., Hickey et al. 2003).

At fortnightly and longer time scales, the vertically integrated temperature time derivative and advective heat flux divergences are of similar magnitude at midshelf locations ($x < -2500$ m; Fig. 12b), with the surface heat flux a factor of 2 smaller. However, in the shallow-water depths of the inner-shelf ($h < 13$ m at $x > -1600$ m; Fig. 12b), a transition occurs where the surface heat flux and vertically integrated advective heat flux principally balance. Farther onshore and into the surfzone, the fortnightly temperature time derivative is less important. This model heat budget on fortnightly and longer time scales from August to October is similar to the summertime Martha's Vineyard inner-shelf heat balance, where surface heat flux and lateral advective terms are in balance on time scales of weeks and months Fewings and Lentz 2011).

In section 6a, the similar observed and modeled $\overline{N}^2/S^2_{\text{rms}}$ suggested that the model was not vertically overmixing and that the underpredicted model velocity shear was suggested to be due to the too weak model stratification. As even on the outer midshelf ($x = -4000$ m; Fig. 12b), the fortnightly and longer surface heat flux is only a factor of 3 smaller than the advective flux. Thus, the too weak model stratification may be due to too weak stratification at the U14 L3 parent grid in addition to too weak surface forcing (which is also used by the U14 parent grids).

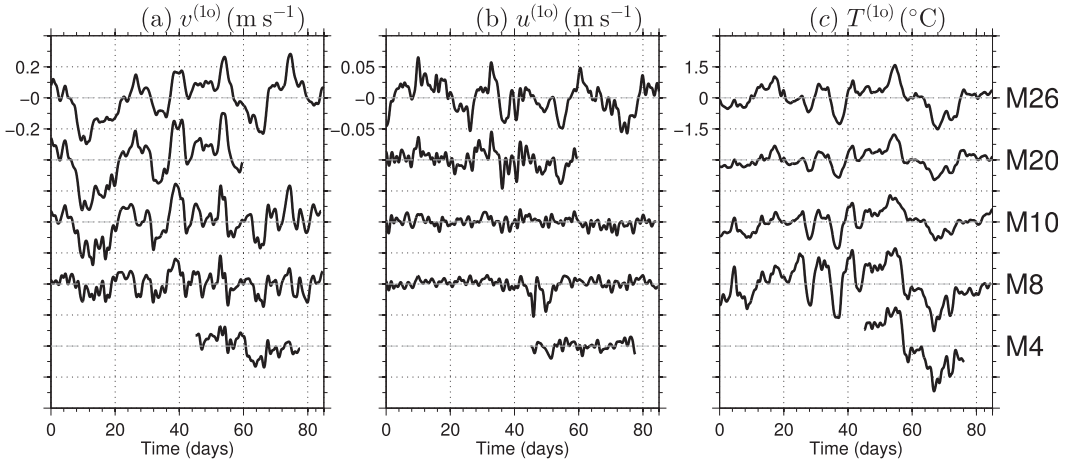

FIG. 13. First EOF, reconstructed, near-surface, observed subtidal (a) cross-shore velocity $u^{(1o)}$, (b) alongshore velocity $v^{(1o)}$, and (c) temperatures $T^{(1o)}$ vs time at midshelves M26 and M20, inner-shelves M10 and M8, and seaward of the surfzone M4. Time t corresponds to days from 1 Aug 2006 (UTC).

c. *Disconnect between surfzone and inner-shelf alongshore currents*

Surfzone alongshore currents (Fig. 6) are driven largely by oblique incident wave forcing, whereas inner-shelf alongshore currents are due to a mix of wind, tidal, and buoyancy forcing and intrinsic variability. This difference results in distinct surfzone and inner-shelf alongshore current variability. At the surfzone M1.5, both observed and modeled v have magnitude up to 0.5 m s^{-1} (Fig. 6d). At the inner-shelf M8, just 280 m offshore in 8-m water depth, the observed and modeled subtidal v_{ST} have much weaker magnitude of $\approx$0.1 m s^{-1} (Figs. 7c,d). The squared correlation between subtidal alongshore currents v_{ST} at M1.5 and (depth averaged) M8 is $r^2 = 0.11$ for the observations and $r^2 = 0.04$ for the model, both not significantly different from zero at 95% confidence. For the unfiltered (i.e., subtidal to high frequency) alongshore current, the squared correlations are essentially zero ($r^2 = 0.01$) for both.

This weak relationship between M1.5 and M8 (cross-shore separated by 280 m) alongshore currents is in contrast to that observed at Duck, North Carolina (Feddersen et al. 1998), but not unexpected. Unlike the U.S. East Coast, in the SPB the alongshore wind stress τ_y and H_s^2 are uncorrelated as the waves are remotely generated 1000 km away. The unrelated surfzone and inner-shelf alongshore currents (separated by 220 m) demonstrate that they have distinct forcing mechanisms and highlight the need for a coupled midshelf to surfzone model that has the relevant wind, wave, tidal, and buoyancy processes together with accurate boundary conditions. Furthermore, this lack of relationship has implications for real-time nearshore plume tracking, as a current real-time system uses HF radar-derived currents from >1 km offshore to extrapolate surfzone alongshore currents (Kim et al. 2009). As shoreline-injected anthropogenic tracers often are surfzone contained for many kilometers along the coast (e.g., Grant et al. 2005), this will result in incorrect plume transport and dispersion estimates.

d. *Cross-shelf coherence of mid- and inner shelf subtidal velocities and temperatures*

Subtidal momentum and temperature can substantially vary from the mid- to inner shelf because of the changing relative importance of momentum (e.g., wind stress, pressure gradient, waves, advection, and eddies) and temperature (e.g., advective and surface heat flux) dynamics. Observed and modeled first vertical EOF, reconstructed, near-surface velocities and temperature [(5a)–(5c)] from mooring location M26–M8 (Fig. 11), together with (just seaward of surfzone) M4 subtidal velocity and temperature, are used to investigate the cross-shelf coherence in the subtidal band. Henceforth, the subscript ST is removed. Also, the superscript 1 refers to the first EOF mode, and the superscripts o and m suggest observed and modeled quantities, respectively.

The observed reconstructed subtidal alongshore velocities $v^{(1o)}$ are coherent from the mid- to inner shelf (Fig. 13a). Between 26- to 10-m depth (M26 to M10), the $v^{(1o)}$ have $r^2 = 0.56$ (Fig. 13a) with a magnitude of $\pm$0.2 m s^{-1}. The $v^{(1o)}$ magnitude decreases in the shallower water of M10 and M8 (Fig. 13a). Although the M4 time series is shorter, $v^{(1o)}$ between M26 and M4 (4-m depth) is reasonably coherent (Fig. 13a) with $r^2 = 0.24$ (significantly different than zero at 95% confidence with 24 degrees of freedom). In contrast, the coherence is zero between inner-shelf M8 and surfzone alongshore currents (section 6c). This pattern of $v^{(1o)}$ cross-shelf

coherence is also seen in the modeled reconstructed subtidal alongshore velocities $v^{(1m)}$. The observed reconstructed cross-shore velocity $u^{(1o)}$ is largely coherent on the midshelf between M26 and M20 with $r^2 = 0.44$ (Fig. 13b). Between the mid- and inner shelf, $u^{(1o)}$ coherence is weaker (M20 and M10 $r^2 = 0.20$), and $u^{(1o)}$ magnitude decreases strongly on the inner shelf. This pattern is similar in modeled $u^{(1m)}$, although the r^2 between mooring locations is slightly higher. Subtidal temperature evolution in the midshelf (M26 and M20) and inner shelf (M10, M8, and M4) have strongly correlated observed reconstructed temperatures $T^{(1o)}$ with $r^2 \geq 0.61$ and magnitude that increases slightly in shallower water (Fig. 13c). The modeled $T^{(1m)}$ correlations across mooring locations are similar.

Observed and modeled reconstructed subtidal velocities and temperatures [$u^{(1)}$, $v^{(1)}$, and $T^{(1)}$; Fig. 13] are subjected to a cross-shore cEOF analysis (section 2b) from M26 to M8 to identify the dominant mode of cross-shore variability and to compare the model to the observations. M4 velocities and temperatures time series are shorter than elsewhere (Fig. 13) and not used in this analysis. The first cross-shore cEOF velocity $\psi_w^{(1)}(x)$ and temperature $\psi_T^{(1)}(x)$ modes explain ≥89% and 97%, respectively, of both the observed and modeled variance. The cross-shore coherent velocity and temperature standard deviation associated with this first mode are

$$\sigma_u^{(1)}(x) = \mathrm{std}\{\mathrm{Re}[B^{(1)}(t)\psi_w^{(1)}(x)]\}, \tag{9a}$$

$$\sigma_v^{(1)}(x) = \mathrm{std}\{\mathrm{Im}[B^{(1)}(t)\psi_w^{(1)}(x)]\}, \tag{9b}$$

$$\sigma_T^{(1)}(x) = \mathrm{std}[B^{(1)}(t)\psi_T^{(1)}(x)]. \tag{9c}$$

Observed $\sigma_v^{(1o)}(x)$ and $\sigma_u^{(1o)}(x)$ (black squares, Figs. 14a and b) have a velocity decrease from the mid- to inner shelf. The cross-shelf coherent velocity std $\sigma_u^{(1o)}(x)$ (black squares, Fig. 14b) is one order of magnitude smaller than those of alongshore velocity $\sigma_v^{(1o)}(x)$ (black squares, Fig. 14a). Modeled $\sigma_v^{(1m)}(x)$ and $\sigma_u^{(1m)}(x)$ estimates are of the same magnitude as observations (red squares, Figs. 14a,b) and closely follow the flow variability decrease from deeper (26 m) to shallower waters (8 m). Observed $\sigma_T^{(1o)}(x)$ (black squares, Fig. 14c) shows increased temperature variability from 20-m depth to shallower waters (8–10-m depth), a trend generally captured by the modeled $\sigma_T^{(1m)}(x)$.

The decrease in modeled and observed near-surface $v^{(1)}$ from the deeper midshelf to shallower inner-shelf has been previously observed (e.g., Lentz and Winant 1986; Lentz et al. 1999; Kirincich and Barth 2009) and is consistent with a larger bottom boundary layer role in shallower water. The coherent mid- to inner-shelf $v^{(1)}$ variability is therefore consistent with subtidal wind forcing, alongshelf pressure gradients, or meso- and submesoscale eddies with length scale ≳ 4 km impinging at the coast. The cross-shelf coherent subtidal temperature variability from the mid- to inner shelf together with the modeled dominance of the advective heat flux (section 6b) indicates the lateral advective fluxes (and divergences) of heat flux are coherent across the 4-km region.

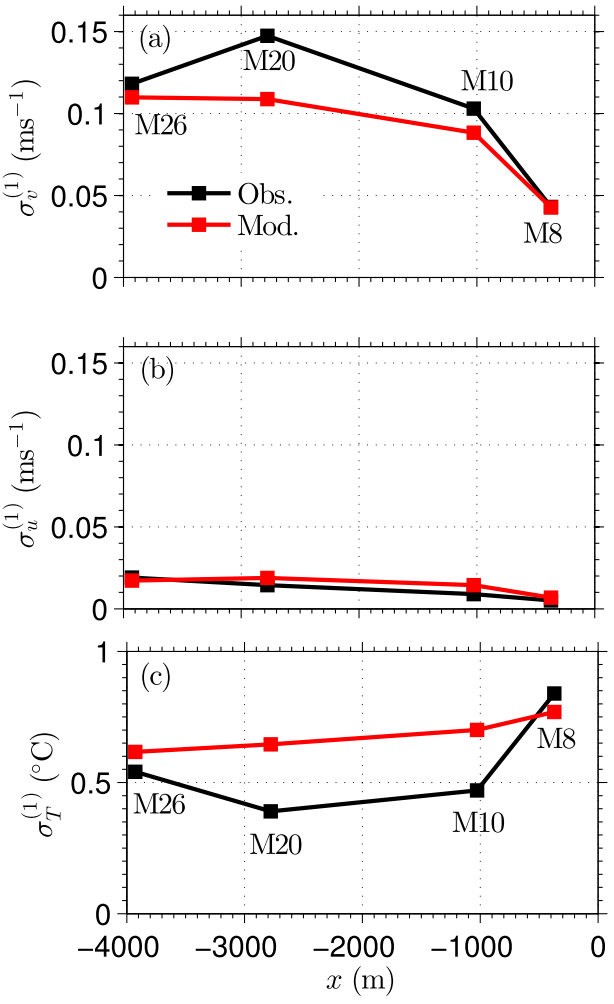

FIG. 14. Cross-shore EOF modes for near-surface (a) alongshore velocity std $\sigma_v^{(1)}(x)$, (b) cross-shore velocity std $\sigma_u^{(1)}(x)$, and (c) temperature $\sigma_T^{(1)}(x)$ vs cross-shore distance x for observed (black) and modeled (red).

Next, the ability of the alongshelf wind stress to drive cross-shelf coherent alongshelf currents is examined. The mid- to inner-shelf–averaged coherent alongshelf current $\mathcal{V}^{(1)}$ as determined from the cross-shore cEOF is

$$\mathcal{V}^{(1)}(t) = \mathrm{Im}[B^{(1)}(t)\langle\psi_w^{(1)}(x)\rangle_x], \tag{10}$$

where $\langle\ \rangle$ is a cross-shelf average from mid- to inner shelf. Assuming a balance between alongshore wind stress and linear bottom stress (Lentz and Winant 1986) yields

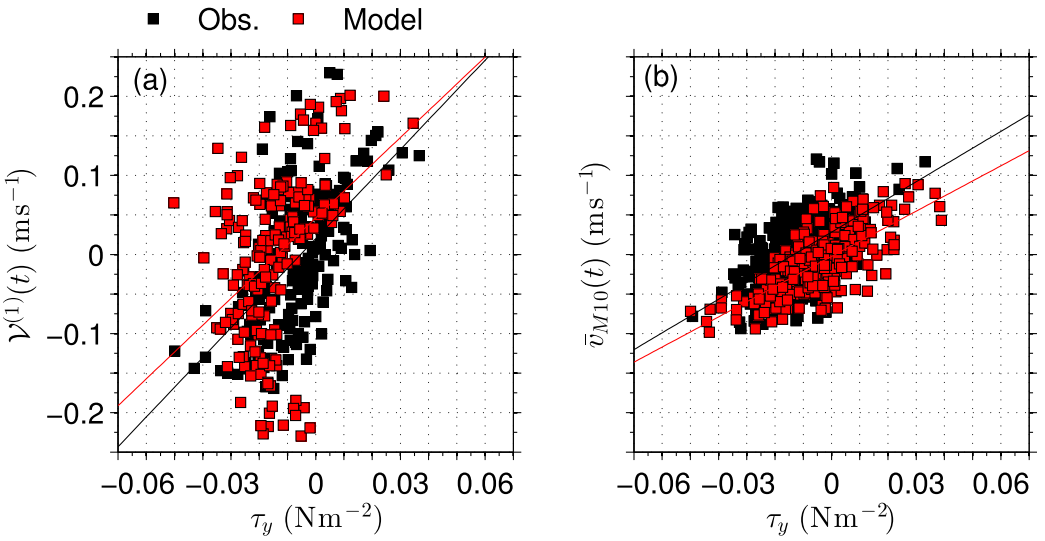

FIG. 15. Observed (black) and modeled (red) (a) alongshore component of the first cross-shore mode $\mathcal{V}^{(1)}$ [(10)] and (b) M10 depth-averaged subtidal alongshore current $\bar{v}$ vs subtidal alongshore wind stress τ_y either observed at N20 or from the WRF Model. The symbols represent subsampling every 8 h. The least-squared best-fit slopes (solid lines) are related to r_f^{-1} [(11)] and yield (observed and modeled) $r_f = (2.9 \pm 0.7, 2.6 \pm 0.4) \times 10^{-4}$ m s^{-1} in (a) and $r_f = (2.6 \pm 0.4, 3.4 \pm 0.4) \times 10^{-4}$ m s^{-1} in (b).

$$r_f \mathcal{V}^{(1)}(t) = \frac{\tau_y}{\rho_0}, \tag{11}$$

where r_f is a linear drag coefficient. Although bottom stress in mixed wave–current environments with variable bottom sediment and roughness is complex, here this simple formulation [(11)] is used to evaluate the observed and modeled cross-shelf coherent subtidal response to wind stress.

Observed $\mathcal{V}^{(1o)}$ is moderately related ($r^2 = 0.25$) to the observed τ_y (Fig. 15a), suggesting that the entire inner to midshelf responds in part to alongshore wind forcing. Modeled $\mathcal{V}^{(1m)}$ is similarly moderately related ($r^2 = 0.36$) to τ_y (red in Fig. 15a). The best-fit slope between τ_y and $\mathcal{V}^{(1)}$ (solid lines in Fig. 15a) gives the best fit r_f via (11). The observed $r_f^{(o)} = 2.6 \times 10^{-4}$ m s^{-1} and modeled $r_f^{(m)} = 2.9 \times 10^{-4}$ m s^{-1} are similar, as are the correlations, suggesting that even though the observed and modeled wind stresses are not coherent, the model is correctly reproducing the relationship between wind stress and velocity.

These bulk (mid- to inner shelf), near-surface r_f values are similar to inner-shelf r_f estimated with the M10 depth-averaged, subtidal alongshore current $\bar{v}$ (overbar represents a depth average) and alongshore wind stress, assuming, similar to (11), $r_f \bar{v} = \tau_y/\rho_0$. In addition, the r_f values estimated here are similar to a range of previously estimated r_f on the outer, mid-, and inner shelf (60–10-m depth) of the SCB (e.g., Lentz and Winant 1986; Hickey et al. 2003). Observed and modeled M10 $\bar{v}$ and τ_y are moderately correlated with $r^2 = 0.30$ and $r^2 = 0.36$, respectively (Fig. 15b). The observed and modeled best-fit M10 linear drag coefficient $r_f^{(o)} = 2.6(\pm 0.4) \times 10^{-4}$ m s^{-1} and $r_f^{(m)} = 3.4\,(\pm 0.4) \times 10^{-4}$ m s^{-1} are similar, again suggesting the model is reproducing the observed wind stress and alongshelf velocity relationship.

e. *Local alongshelf wind forcing in the San Pedro Bay inner shelf*

The subtidal depth-averaged alongshore current $\bar{v}$ variability in San Pedro basin explained by local wind forcing is explored in both observations and model through a simple, local, depth-averaged, alongshore momentum balance between local acceleration, wind stress, and bottom stress (e.g., Lentz and Winant 1986; Lentz et al. 1999; Fewings and Lentz 2010; Kumar et al. 2013):

$$\frac{\partial \bar{v}_{\rm lp}}{\partial t} + \frac{r_f}{h}\bar{v}_{\rm lp} = \frac{\tau_y}{\rho_0 h}, \tag{12}$$

where $\bar{v}_{\rm lp}$ is the wind-driven local-predicted $\bar{v}$. Coriolis force is neglected in (12), assuming that the frictional time scales ($T_f = h/r_f$) are much shorter than rotational time scales ($T_r = 2\pi/f$). The balance (12) has a closed-form solution for $\bar{v}_{\rm lp}$:

$$\bar{v}_{\rm lp}(t) = \int_0^t \left(\frac{\tau_y}{\rho_0 h}\right) e^{-(t-t')/T_f}\, dt' + \bar{v}_0 e^{-t/T_f}, \tag{13}$$

where $\bar{v}_0$ is the initial condition at $t = 0$ (Lentz and Winant 1986).

The observed and modeled local-predicted $\overline{v}_{\rm lp}$ is calculated at M10 with (13) using the observed and modeled wind stress, initial conditions, and the appropriate best-fit r_f, respectively (Fig. 15b). The resulting $T_f \approx 10$ h, less than the rotational time scale of ≈22 h. These local-predicted subtidal depth-averaged alongshelf currents for the observed and modeled $\overline{v}_{\rm lp}^{(o)}$ and $\overline{v}_{\rm lp}^{(m)}$ are compared to observed $\overline{v}^{(o)}$ and modeled $\overline{v}^{(m)}$, respectively (Fig. 16). Observed local-predicted $\overline{v}_{\rm lp}^{(o)}$ is moderately related to $\overline{v}^{(o)}$ (Fig. 16a) with squared correlation $r^2 = 0.42$, RMSE $= 0.06\,{\rm m\,s^{-1}}$, and a best-fit slope of 0.48(±0.06). The modeled local-predicted along-shelf current $\overline{v}_{\rm lp}^{(m)}$ also is moderately related to $\overline{v}^{(m)}$ (Fig. 16b) with squared correlation $r^2 = 0.46$, RMSE $= 0.05\,{\rm m\,s^{-1}}$, and best-fit slope 0.44(±0.06).

The relationship between $\overline{v}$ and $\overline{v}_{\rm lp}$ is similar for both observed and modeled, suggesting that the model accurately represents the partially wind-forced subtidal circulation dynamics. Thus, other alongshore momentum dynamics (e.g., alongshore pressure gradients, mean advective terms, meso- and submesoscale eddies) must also play a significant role on the inner shelf, consistent with previously reported inner-shelf alongshore current response in the SCB (Lentz and Winant 1986).

f. *Inner-shelf alongshelf nonuniformity*

Nonuniform alongshelf subtidal currents can occur because of nonuniform bathymetry; varying offshore flows (from boundary conditions); differences in wind, wave, or pressure gradient forcing; and intrinsically generated variability. Alongshelf nonuniform currents have a dynamical effect not included in local wind-driven balances [(12)]. At the HB06 site, the bathymetry is largely alongshelf uniform (Figs. 1a, 2d) on a scale of 5–10 km, although the coastline bends at $y = 3.5$ km. On a larger spatial scale (Figs. 2b,c), the shelf break is wider farther to northwest ($+y$) leading into Palos Verdes that bounds the San Pedro Bay. To the southeast ($-y$), the shelf break narrows from 10 to 2 km (Fig. 2c). This larger-scale variation, which is outside the smallest L5 grid domain, suggests that alongshelf effects may be important.

Here, nonuniformity in the observed and modeled inner-shelf, subtidal, depth-averaged, alongshelf current $\overline{v}$ is quantified at M10 and N10, separated by 4 km on the same isobath (see Fig. 1a). Observed depth-averaged subtidal $\overline{v}$ at M10 and N10 [i.e., $\overline{v}_{\rm M10}^{(o)}$ and $\overline{v}_{\rm N10}^{(o)}$] are strongly correlated ($r^2 = 0.86$) and vary in magnitude between $\pm 0.25\,{\rm m\,s^{-1}}$ (Fig. 17a). The observed alongshore $\overline{v}$ difference [i.e., $\Delta\overline{v}^{(o)} = \overline{v}_{\rm N10}^{(o)} - \overline{v}_{\rm M10}^{(o)}$; Fig. 17c] is generally small ($<0.05\,{\rm m\,s^{-1}}$) relative to $\overline{v}^{(o)}$, with $\Delta\overline{v}^{(o)}$ mean and standard deviation of ≈ -0.02 and $0.04\,{\rm m\,s^{-1}}$, respectively. Modeled depth-averaged subtidal flows at M10 and N10 [$\overline{v}_{\rm M10}^{(m)}$ and $\overline{v}_{\rm N10}^{(m)}$] are strongly correlated

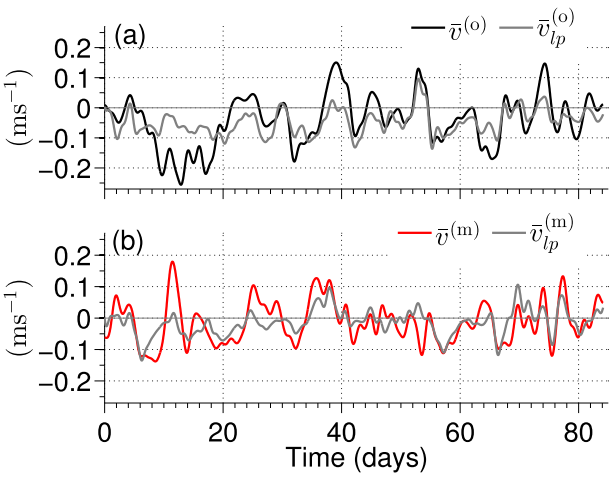

FIG. 16. (a) Observed $\overline{v}^{(o)}$ (black) and local-predicted $\overline{v}_{\rm lp}^{(o)}$ (gray) and (b) modeled $\overline{v}^{(m)}$ (red) and local-predicted $\overline{v}_{\rm lp}^{(m)}$ (gray) subtidal, depth-averaged, alongshore velocity vs time at M10. Local-predicted $\overline{v}_{\rm lp}$ in (a) and (b) are derived from (13). Observed $\overline{v}^{(o)}$ and predicted $\overline{v}_{\rm lp}^{(o)}$ are moderately correlated ($r^2 = 0.42$) with a best-fit line slope $m = 0.48 \pm 0.06$. Correlation between model-simulated $\overline{v}^{(m)}$ and WRF wind-predicted $\overline{v}_{\rm lp}^{(m)}$ is $r^2 = 0.46$ and $m = 0.44 \pm 0.06$. Time corresponds to days from 1 Aug 2006 (UTC).

$r^2 = 0.75$ and have variability similar to the observations (Fig. 17b). Modeled $\Delta\overline{v}^{(m)}$ has a similar mean ($\approx -0.02\,{\rm m\,s^{-1}}$) and standard deviation ($\approx 0.04\,{\rm m\,s^{-1}}$) as the observed $\Delta\overline{v}^{(o)}$ (Fig. 17d).

The observed and modeled $\overline{v}$ alongshelf nonuniformity on the inner shelf are similar (Fig. 17), suggesting that the model with one-way grid nesting (section 3b) is correctly capturing the alongshelf variable dynamics. These $\Delta\overline{v}$ results also allow for the quantification of alongshelf advection effects in the local alongshelf dynamics [(12)]. As the alongshelf advection $\overline{v}\partial\overline{v}/\partial y$ and the bottom friction $(r_f/h)\overline{v}$ dynamical terms are $\propto\overline{v}$, the two terms can be compared by considering their typical inverse time scale. For alongshelf advection, a typical $\Delta\overline{v} = 0.04\,{\rm m\,s^{-1}}$ over $L_y = 4000$ m yields an alongshelf inverse time scale of $T_y = \Delta\overline{v}/L_y = 10^{-5}\,{\rm s^{-1}}$, which is ⅓ of the inverse frictional time scale $T_f = r_f/h \approx 3 \times 10^{-5}\,{\rm s^{-1}}$. This indicates that although smaller than the bottom stress, the alongshelf advection is not negligible in the alongshelf dynamics in $h = 10$-m depth and may partially account for the differences between $\overline{v}$ and $\overline{v}_{\rm lp}$ in both the observations and the model (Fig. 16).

g. *Wind- versus wave-induced cross-shelf transport*

In the midshelf, cross-shelf Ekman transport driven by alongshelf wind stress, that is, $U_E = \tau_y/\rho_0 f$, where f is the Coriolis parameter, is an important cross-shelf exchange mechanism (e.g., Lentz 1992; Shearman and Lentz 2003) along with eddy fluxes (e.g., Marchesiello et al. 2003). In

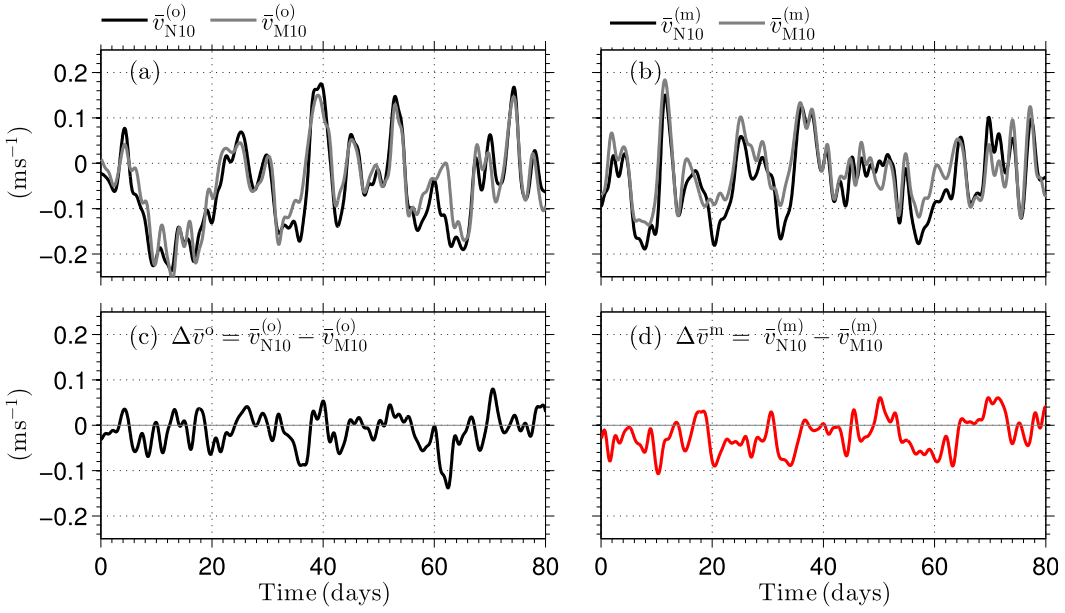

FIG. 17. (a) Observed $\bar{v}^{(o)}$ and (b) modeled $\bar{v}^{(m)}$ depth-averaged, subtidal, alongshore current at N10 (black) and M10 (gray) vs time. Alongshore current difference $\Delta\bar{v}$ between M10 and N10 for (c) observed ($\Delta\bar{v}^{(o)} = \bar{v}^{(o)}_{N10} - \bar{v}^{(o)}_{M10}$) and (d) modeled ($\Delta\bar{v}^{(m)} = \bar{v}^{(m)}_{N10} - \bar{v}^{(m)}_{M10}$) vs time. Time corresponds to days from 1 Aug 2006 (UTC).

shallow waters ($h < 15$ m), the Ekman transport is diminished where the surface and bottom boundary layers are not distinct, limiting the potential for cross-shelf exchange. On the inner-shelf, the wave-induced cross-shore Stokes transport (e.g., McWilliams and Restrepo 1999) $Q_w = gH_s^2\cos(\bar{\theta})/16c$, where c is the surface gravity wave speed, can be of the same order as cross-shelf Ekman transport (e.g., Lentz et al. 2008). However, wave-driven Stokes transport only induces cross-shelf exchange when the Eulerian return flow does not balance the onshore Stokes drift because of, for example, strong vertical mixing (e.g., Lentz et al. 2008).

Nevertheless, the relative potential of wave-induced versus wind-induced transport in cross-shelf exchange can be diagnosed by the ratio of wave-driven to Ekman cross-shore transport (e.g., Lentz et al. 2008):

$$R_{wE} = \frac{Q_w}{U_E} = \frac{\rho_0 gf}{16c}\frac{H_s^2\cos(\bar{\theta})}{\tau_y}, \qquad (14)$$

which is calculated on each cross-shore transect location (Fig. 1b) using the observed N20 alongshelf subtidal wind stress, model significant wave height H_s, mean direction $\bar{\theta}$, and linear theory phase speed c (estimated from model mean wave period; Fig. 5b). Note that small wind stresses with magnitude one standard deviation less than mean wind stress were not included in this analysis.

In general, mean R_{wE} (solid black, Fig. 18) increases from the midshelf to the surfzone mainly because of decrease in the phase speed c. In the midshelf ($x = -4000$ m; Fig. 18), mean $R_{wE} \approx 0.2$. At cross-shore locations farther inshore (e.g., $x = -800$ m, $h = 10$ m), $R_{wE} \approx 0.3$, and in even shallower waters, R_{wE} substantially increases, suggesting that wave-induced transport is almost of the same order as wind-induced transport. Although the wind stress τ_y and H_s^2 are uncorrelated, the relative magnitudes of wind stress and waves can be compared. The mean (±standard deviation) of $H_s^2/\tau_y = 60(\pm 50)$ m^4 N^{-1} is larger than the U.S. East

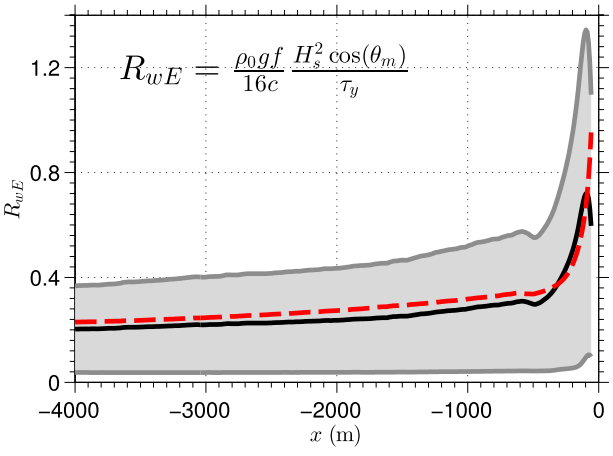

FIG. 18. The ratio of wave-driven to Ekman-driven cross-shelf transport R_{wE} for mean (solid black curve) and std (gray shading) vs cross-shore distance x. The predicted (14) ratio R_{wE} using $H_s^2/\tau_y = 60$ m^4 N^{-1} and $T_m = 10$ s is given by the red-dashed curve.

Coast value $H_s^2/\tau_y = 25\,\mathrm{m^4\,N^{-1}}$ (Lentz et al. 2008). Using $H_s^2/\tau_y = 60\,\mathrm{m^4\,N^{-1}}$, $\overline{\theta} = 0°$, and the mean wave period $T_m = 10\,\mathrm{s}$, the parameterized R_{wE} closely matches the mean R_{wE} at all cross-shelf locations (cf. red dashed with black in Fig. 18), suggesting that this simple expression based on the mean H_s^2/τ_y ratio and a constant mean period is useful in diagnosing the relative potential of wave versus wind-induced cross-shelf exchange.

The observed and modeled Eulerian mean cross-shore velocity on the mid- and inner shelf (Figs. 9a$_2$–e$_2$) does not have a surface-intensified Stokes–Coriolis-driven Eulerian return flow to balance the onshore-directed Stokes drift transport that has been observed in the shelf region of U.S. East Coast (e.g., Lentz et al. 2008) and idealized modeling studies (e.g., Kumar et al. 2012), suggesting that the cross-shelf dynamics are much more complex than the idealized dynamics in Lentz et al. (2008). Diagnosing the detailed relative importance of wind- and wave-driven cross-shelf exchange processes is complex requiring analysis of momentum balances.

7. Summary

Accurately simulating cross-shore exchange from the surfzone to the midshelf requires a coupled wave and circulation model that includes tide, wind, buoyancy, and wave processes. The COAWST modeling system with coupled ROMS and SWAN includes all these processes, yet has not been extensively validated jointly from the midshelf to surfzone. Here, COAWST is applied to the midshelf to surfzone region of San Pedro Bay, with wave, surface forcing, and temperature, and velocity lateral boundary conditions are provided by other models. To test the model for use in studying cross-shelf exchange, modeled tides, waves, velocities, and temperatures are compared, primarily statistically, to field measurements from the Huntington Beach 2006 experiment.

In 8-m water depth, diurnal tidal constituents are well modeled, although semidiurnal tidal constituents are underestimated by ≈1/3. Modeled wave parameters (e.g., wave height, mean wave period) favorably compare to the observations both seaward of (4-m depth) and within the surfzone (1.5-m depth). Modeled cross- and alongshore currents, both seaward and within the surfzone (i.e., M3 and M1.5, respectively), are reasonably well reproduced, particularly given the differences in observed and modeled surfzone bathymetry. In the mid- (26-m depth) and inner shelf (8-m depth), observed alongshore subtidal velocities and temperature have qualitatively similar variability. However, the observed and modeled shelf currents and temperature are uncorrelated because of the lack of synoptically accurate surface forcing and lateral boundary conditions and because of intrinsic variability, motivating statistical model data comparison.

The modeled, time-averaged cross- and alongshore velocity and surface temperature compare favorably to the observations. However, the modeled alongshore current vertical shear and stratification is weaker than those observed. Modeled and observed midwater column rotary velocity in the midshelf, inner shelf, and surfzone compare favorably in all but the high-frequency band ($>10^{-1}$ cph). Midwater column temperature spectra are well reproduced in the subtidal band at all locations but underpredicted in the diurnal and semidiurnal possibly because of weaker modeled stratification. Both modeled and observed subtidal variance ellipses from the first cEOF reconstructed velocities are strongly polarized with the major velocity axis about 4 times the minor axis. Observed and modeled first EOF reconstructed temperatures are similar with largely depth uniform variability.

The observed and modeled ratio of mean stratification to root-mean-square subtidal velocity vertical shear ($\overline{N}^2/S^2_{\mathrm{rms}}$) in the mid- and inner shelf are similar, suggesting that the model is not overmixing and that with the correct stratification the model subtidal velocity shear would be similar to the observed. At synoptic time scales, the vertically integrated heat budget is a balance between temperature time derivative and advective heat flux divergence at all mid- and inner-shelf locations. At fortnightly and longer time scales, the inner-shelf and surfzone vertically integrated heat budget is largely a balance between surface forcing and advective heat flux, consistent with prior inner-shelf studies. The surfzone and inner-shelf alongshore currents separated by 220 m are essentially unrelated unlike the U.S. East Coast. Observed first cEOF (EOF) reconstructed surface alongshore velocities (surface temperature) are coherent from the inner to midshelf, suggesting coherent cross-shelf subtidal momentum and heat forcing. The model has a similar pattern of alongshore velocity and temperature coherence.

The depth-averaged alongshore currents in 10-m depth, predicted from simple dynamics of wind forcing, bottom stress with best-fit linear drag coefficient, and local acceleration, explains ≈50% of both observed and modeled subtidal, depth-averaged $\overline{v}$. Thus, other dynamical processes contribute about half the $\overline{v}$ variance in both the observations and model. In 10-m water depth, the observed and modeled alongshore nonuniform $\overline{v}$ are statistically similar, and alongshore advection in the inner shelf is ≈1/3 of the wind forcing. The relative role of Stokes to Ekman transport, an indicator of wave-induced versus wind-induced transport, is found to be stronger in water depths less than 15 m and also

larger than those estimated for the U.S. East Coast. The general success of the temporal, vertical, and cross-shelf statistical model data comparison show that the coupled SWAN and ROMS models well represent the range of tidal, wind, buoyancy, and wave processes from the midshelf to the surfzone.

Acknowledgments. Support for N. Kumar and F. Feddersen was provided by the Office of Naval Research (ONR). W. O'Reilly was supported by the California State Parks. J. McWilliams was supported by ONR N000141410626 and National Science Foundation OCE-1355970. Y. Uchiyama acknowledges Grant-In-Aid for Scientific Research C24560622. Data for the HB06 experiment were obtained within the framework of the Southern California Coastal Ocean Observing System (SCCOOS), National Oceanic and Atmospheric Administration (NOAA), Orange County Sanitation District (OCSD), and United States Geological Survey (USGS) programs at Huntington Beach. Thank you to George Robertson and Marlene Noble for the moored instrument data and to CDIP for the wave data. B. Woodward, B. Boyd, K. Smith, D. Darnell, I. Nagy, D. Clark, M. Omand, M. Rippy, M. McKenna, M. Yates, R.T. Guza, and D. Michrowski provided field support. Corey Olfe, Daniel Dauhajre, and Florian Lemarie prepared the boundary condition information required for model simulations. Computational support was provided by the COMPAS/ATLAS cluster maintained by Caroline Papadopoulos and Bruce Cornuelle. M. Olabarrieta, M. Omand, M. S. Spydell, S. H. Suanda, and Bruce Cornuelle provided useful feedback.

REFERENCES

Anderson, D. M., 2009: Approaches to monitoring, control and management of harmful algal blooms (HABs). *Ocean Coastal Manage.,* **52,** 342–347, doi:10.1016/j.ocecoaman.2009.04.006.

Austin, J. A., and S. J. Lentz, 2002: The inner shelf response to wind-driven upwelling and downwelling. *J. Phys. Oceanogr.,* **32,** 2171–2193, doi:10.1175/1520-0485(2002)032<2171:TISRTW>2.0.CO;2.

Battjes, J., and J. Janssen, 1978: Energy loss and set-up due to breaking of random waves. *Proc. 16th Conf. on Coastal Engineering,* Hamburg, Germany, ASCE, 569–587.

Beckenbach, E., and E. Terrill, 2008: Internal tides over abrupt topography in the Southern California Bight: Observations of diurnal waves poleward of the critical latitude. *J. Geophys. Res.,* **113,** C02001, doi:10.1029/2006JC003905.

Becker, J., and Coauthors, 2009: Global bathymetry and elevation data at 30 arc seconds resolution: SRTM30_PLUS. *Mar. Geod.,* **32,** 355–371, doi:10.1080/01490410903297766.

Boé, J., A. Hall, F. Colas, J. C. McWilliams, X. Qu, J. Kurian, and S. B. Kapnick, 2011: What shapes mesoscale wind anomalies in coastal upwelling zones? *Climate Dyn.,* **36,** 2037–2049, doi:10.1007/s00382-011-1058-5.

Booij, N., R. Ris, and L. H. Holthuijsen, 1999: A third-generation wave model for coastal regions: 1. Model description and validation. *J. Geophys. Res.,* **104,** 7649–7666, doi:10.1029/98JC02622.

Buijsman, M., Y. Uchiyama, J. McWilliams, and C. Hill-Lindsay, 2012: Modeling semidiurnal internal tide variability in the Southern California Bight. *J. Phys. Oceanogr.,* **42,** 62–77, doi:10.1175/2011JPO4597.1.

Businger, J. A., J. C. Wyngaard, Y. Izumi, and E. F. Bradley, 1971: Flux-profile relationships in the atmospheric surface layer. *J. Atmos. Sci.,* **28,** 181–189, doi:10.1175/1520-0469(1971)028<0181:FPRITA>2.0.CO;2.

Caldwell, R., L. Taylor, B. Eakins, K. Carignan, P. Grothe, E. Lim, and D. Friday, 2011: Digital elevation models of Santa Monica, California: Procedures, data sources and analysis. NOAA Tech. Memo. NESDIS NGDC-46, 38 pp. [Available online at http://docs.lib.noaa.gov/noaa_documents/NESDIS/NGDC/TM/NOAA_TM_NESDIS_NGDC_46.pdf.]

Capet, X., J. McWilliams, M. Molemaker, and A. Shchepetkin, 2008: Mesoscale to submesoscale transition in the California Current System. Part III: Energy balance and flux. *J. Phys. Oceanogr.,* **38,** 2256–2269, doi:10.1175/2008JPO3810.1.

Capps, S. B., A. Hall, and M. Hughes, 2014: Sensitivity of Southern California wind energy to turbine characteristics. *Wind Energy,* **17,** 141–159, doi:10.1002/we.1570.

Carton, J. A., and B. S. Giese, 2008: A reanalysis of ocean climate using Simple Ocean Data Assimilation (SODA). *Mon. Wea. Rev.,* **136,** 2999–3017, doi:10.1175/2007MWR1978.1.

Castelle, B., A. Reniers, and J. MacMahan, 2014: Bathymetric control of surf zone retention on a rip-channelled beach. *Ocean Dyn.,* **64,** 1221–1231, doi:10.1007/s10236-014-0747-0.

Chapman, D. C., 1985: Numerical treatment of cross-shelf open boundaries in a barotropic coastal ocean model. *J. Phys. Oceanogr.,* **15,** 1060–1075, doi:10.1175/1520-0485(1985)015<1060:NTOCSO>2.0.CO;2.

Clark, D. B., F. Feddersen, and R. T. Guza, 2010: Cross-shore surfzone tracer dispersion in an alongshore current. *J. Geophys. Res.,* **115,** C10035, doi:10.1029/2009JC005683.

——, ——, and ——, 2011: Modeling surfzone tracer plumes: 2. Transport and dispersion. *J. Geophys. Res.,* **116,** C11028, doi:10.1029/2011JC007211.

——, S. Elgar, and B. Raubenheimer, 2012: Vorticity generation by short-crested wave breaking. *Geophys. Res. Lett.,* **39,** L24604, doi:10.1029/2012GL054034.

Conil, S., and A. Hall, 2006: Local regimes of atmospheric variability: A case study of Southern California. *J. Climate,* **19,** 4308–4325, doi:10.1175/JCLI3837.1.

Craik, A., and S. Leibovich, 1976: A rational model for Langmuir circulations. *J. Fluid Mech.,* **73,** 401–426, doi:10.1017/S0022112076001420.

Dong, C., E. Y. Idica, and J. C. McWilliams, 2009: Circulation and multiple-scale variability in the Southern California Bight. *Prog. Oceanogr.,* **82,** 168–190, doi:10.1016/j.pocean.2009.07.005.

Egbert, G. D., A. F. Bennett, and M. G. Foreman, 1994: TOPEX/Poseidon tides estimated using a global inverse model. *J. Geophys. Res.,* **99,** 24 821–24 852, doi:10.1029/94JC01894.

Feddersen, F., 2004: Effect of wave directional spread on the radiation stress: Comparing theory and observations. *Coastal Eng.,* **51,** 473–481, doi:10.1016/j.coastaleng.2004.05.008.

——, 2012: Observations of the surf-zone turbulent dissipation rate. *J. Phys. Oceanogr.,* **42,** 386–399, doi:10.1175/JPO-D-11-082.1.

——, 2014: The generation of surfzone eddies in a strong alongshore current. *J. Phys. Oceanogr.,* **44,** 600–617, doi:10.1175/JPO-D-13-051.1.

——, R. T. Guza, S. Elgar, and T. H. C. Herbers, 1998: Alongshore momentum balances in the nearshore. *J. Geophys. Res.,* **103,** 15 667–15 676, doi:10.1029/98JC01270.

——, ——, ——, and ——, 2000: Velocity moments in alongshore bottom stress parameterizations. *J. Geophys. Res.,* **105,** 8673–8686, doi:10.1029/2000JC900022.

——, D. B. Clark, and R. T. Guza, 2011: Modeling of surfzone tracer plumes: 1. Waves, mean currents, and low-frequency eddies. *J. Geophys. Res.,* **116,** C11027, doi:10.1029/2011JC007210.

Fewings, M. R., and S. J. Lentz, 2010: Momentum balances on the inner continental shelf at Martha's Vineyard Coastal Observatory. *J. Geophys. Res.,* **115,** C12023, doi:10.1029/2009JC005578.

——, and ——, 2011: Summertime cooling of the shallow continental shelf. *J. Geophys. Res.,* **116,** C07015, doi:10.1029/2010JC006744.

——, ——, and J. Fredericks, 2008: Observations of cross-shelf flow driven by cross-shelf winds on the inner continental shelf. *J. Phys. Oceanogr.,* **38,** 2358–2378, doi:10.1175/2008JPO3990.1.

Flather, R., 1976: A tidal model of the northwest European continental shelf. *Mem. Soc. Roy. Sci. Liege,* **10,** 141–164.

Ganju, N. K., S. J. Lentz, A. R. Kirincich, and J. T. Farrar, 2011: Complex mean circulation over the inner shelf south of Martha's Vineyard revealed by observations and a high-resolution model. *J. Geophys. Res.,* **116,** C10036, doi:10.1029/2011JC007035.

Garcez Faria, A., E. Thornton, T. Lippmann, and T. Stanton, 2000: Undertow over a barred beach. *J. Geophys. Res.,* **105,** 16 999–17 010, doi:10.1029/2000JC900084.

Geyer, W. R., and R. Signell, 1990: Measurements of tidal flow around a headland with a shipboard acoustic Doppler current profiler. *J. Geophys. Res.,* **95,** 3189–3197, doi:10.1029/JC095iC03p03189.

Giddings, S., and Coauthors, 2014: Hindcasts of potential harmful algal bloom transport pathways on the Pacific Northwest coast. *J. Geophys. Res. Oceans,* **119,** 2439–2461, doi:10.1002/2013JC009622.

Gonella, J., 1972: A rotary-component method for analysing meteorological and oceanographic vector time series. *Deep-Sea Res. Oceanogr. Abstr.,* **19,** 833–846, doi:10.1016/0011-7471(72)90002-2.

Grant, S. B., J. H. Kim, B. H. Jones, S. A. Jenkins, J. Wasyl, and C. Cudaback, 2005: Surf zone entrainment, along-shore transport, and human health implications of pollution from tidal outlets. *J. Geophys. Res.,* **110,** C10025, doi:10.1029/2004JC002401.

Haidvogel, D. B., and Coauthors, 2008: Ocean forecasting in terrain-following coordinates: Formulation and skill assessment of the regional ocean modeling system. *J. Comput. Phys.,* **227,** 3595–3624, doi:10.1016/j.jcp.2007.06.016.

Hally-Rosendahl, K., F. Feddersen, and R. T. Guza, 2014: Cross-shore tracer exchange between the surfzone and inner-shelf. *J. Geophys. Res. Oceans,* **119,** 4367–4388, doi:10.1002/2013JC009722.

Herbers, T., S. Elgar, and R. T. Guza, 1999: Directional spreading of waves in the nearshore. *J. Geophys. Res.,* **104,** 7683–7693, doi:10.1029/1998JC900092.

Hickey, B. M., 1992: Circulation over the Santa Monica-San Pedro basin and shelf. *Prog. Oceanogr.,* **30,** 37–115, doi:10.1016/0079-6611(92)90009-O.

——, E. Dobbins, and S. E. Allen, 2003: Local and remote forcing of currents and temperature in the central Southern California Bight. *J. Geophys. Res.,* **108,** 3081, doi:10.1029/2000JC000313.

Huang, H.-Y., S. B. Capps, S.-C. Huang, and A. Hall, 2013: Downscaling near-surface wind over complex terrain using a physically-based statistical modeling approach. *Climate Dyn.,* **44,** 529–542, doi:10.1007/s00382-014-2137-1.

Johnson, D., and C. Pattiaratchi, 2006: Boussinesq modelling of transient rip currents. *Coastal Eng.,* **53,** 419–439, doi:10.1016/j.coastaleng.2005.11.005.

Kim, S. Y., E. J. Terrill, and B. D. Cornuelle, 2009: Assessing coastal plumes in a region of multiple discharges: The U.S.–Mexico border. *Environ. Sci. Technol.,* **43,** 7450–7457, doi:10.1021/es900775p.

Kirby, J. T., and T.-M. Chen, 1989: Surface waves on vertically sheared flows: Approximate dispersion relations. *J. Geophys. Res.,* **94,** 1013–1027, doi:10.1029/JC094iC01p01013.

Kirincich, A. R., and J. A. Barth, 2009: Alongshelf variability of inner-shelf circulation along the central Oregon coast during summer. *J. Phys. Oceanogr.,* **39,** 1380–1398, doi:10.1175/2008JPO3760.1.

——, S. J. Lentz, and J. A. Barth, 2009: Wave-driven inner-shelf motions on the Oregon coast. *J. Phys. Oceanogr.,* **39,** 2942–2956, doi:10.1175/2009JPO4041.1.

Kuik, A. J., G. P. V. Vledder, and L. H. Holthuijsen, 1988: A method for the routine analysis of pitch-and-roll buoy wave data. *J. Phys. Oceanogr.,* **18,** 1020–1034, doi:10.1175/1520-0485(1988)018<1020:AMFTRA>2.0.CO;2.

Kumar, N., G. Voulgaris, and J. C. Warner, 2011: Implementation and modification of a three-dimensional radiation stress formulation for surf zone and rip-current applications. *Coastal Eng.,* **58,** 1097–1117, doi:10.1016/j.coastaleng.2011.06.009.

——, ——, ——, and M. Olabarrieta, 2012: Implementation of the vortex force formalism in the coupled ocean-atmosphere-wave-sediment transport (COAWST) modeling system for inner shelf and surf zone applications. *Ocean Modell.,* **47,** 65–95, doi:10.1016/j.ocemod.2012.01.003.

——, ——, J. H. List, and J. C. Warner, 2013: Alongshore momentum balance analysis on a cuspate foreland. *J. Geophys. Res. Oceans,* **118,** 5280–5295, doi:10.1002/jgrc.20358.

Kundu, P. K., and J. Allen, 1976: Some three-dimensional characteristics of low-frequency current fluctuations near the Oregon coast. *J. Phys. Oceanogr.,* **6,** 181–199, doi:10.1175/1520-0485(1976)006<0181:STDCOL>2.0.CO;2.

Large, W., and S. Pond, 1981: Open ocean momentum flux measurements in moderate to strong winds. *J. Phys. Oceanogr.,* **11,** 324–336, doi:10.1175/1520-0485(1981)011<0324:OOMFMI>2.0.CO;2.

——, J. Morzel, and G. Crawford, 1995: Accounting for surface wave distortion of the marine wind profile in low-level ocean storms wind measurements. *J. Phys. Oceanogr.,* **25,** 2959–2971, doi:10.1175/1520-0485(1995)025<2959:AFSWDO>2.0.CO;2.

Laudien, J., T. Brey, and W. E. Arntz, 2001: Reproduction and recruitment patterns of the surf clam *Donax serra* (Bivalvia, Donacidae) on two Namibian sandy beaches. *S. Afr. J. Mar. Sci.,* **23,** 53–60, doi:10.2989/025776101784528980.

Lentz, S. J., 1992: The surface boundary layer in coastal upwelling regions. *J. Phys. Oceanogr.,* **22,** 1517–1539, doi:10.1175/1520-0485(1992)022<1517:TSBLIC>2.0.CO;2.

——, and C. Winant, 1986: Subinertial currents on the southern California shelf. *J. Phys. Oceanogr.,* **16,** 1737–1750, doi:10.1175/1520-0485(1986)016<1737:SCOTSC>2.0.CO;2.

——, and M. R. Fewings, 2012: The wind- and wave-driven inner-shelf circulation. *Annu. Rev. Mar. Sci.,* **4,** 317–343, doi:10.1146/annurev-marine-120709-142745.

——, R. T. Guza, S. Elgar, F. Feddersen, and T. H. C. Herbers, 1999: Momentum balances on the North Carolina inner shelf. *J. Geophys. Res.,* **104,** 18 205–18 240, doi:10.1029/1999JC900101.

——, M. Carr, and T. Herbers, 2001: Barotropic tides on the North Carolina shelf. *J. Phys. Oceanogr.,* **31,** 1843–1859, doi:10.1175/1520-0485(2001)031<1843:BTOTNC>2.0.CO;2.

——, M. Fewings, P. Howd, J. Fredericks, and K. Hathaway, 2008: Observations and a model of undertow over the inner continental shelf. *J. Phys. Oceanogr.,* **38,** 2341–2357, doi:10.1175/2008JPO3986.1.

Lerczak, J. A., M. Hendershott, and C. Winant, 2001: Observations and modeling of coastal internal waves driven by a diurnal sea breeze. *J. Geophys. Res.,* **106,** 19 715–19 729, doi:10.1029/2001JC000811.

Limeburner, R., and Coauthors, 1985: CODE-2: Moored array and large-scale data report. WHOI Tech. Rep. 85-35/CODE Tech. Rep. 38, 234 pp.

Longuet-Higgins, M. S., 1970: Longshore currents generated by obliquely incident sea waves: 1. *J. Geophys. Res.,* **75,** 6778–6789, doi:10.1029/JC075i033p06778.

Lucas, A., P. Franks, and C. Dupont, 2011: Horizontal internal-tide fluxes support elevated phytoplankton productivity over the inner continental shelf. *Limnol. Oceanogr. Fluids Environ.,* **1,** 56–74, doi:10.1215/21573698-1258185.

Mackinnon, J. A., and M. C. Gregg, 2005: Spring mixing: Turbulence and internal waves during restratification on the New England shelf. *J. Phys. Oceanogr.,* **35,** 2425–2443, doi:10.1175/JPO2821.1.

Marchesiello, P., J. C. McWilliams, and A. Shchepetkin, 2001: Open boundary conditions for long-term integration of regional oceanic models. *Ocean Modell.,* **3,** 1–20, doi:10.1016/S1463-5003(00)00013-5.

——, ——, and ——, 2003: Equilibrium structure and dynamics of the California Current System. *J. Phys. Oceanogr.,* **33,** 753–783, doi:10.1175/1520-0485(2003)33<753:ESADOT>2.0.CO;2.

Martel, A., and F. Chia, 1991: Drifting and dispersal of small bivalves and gastropods with direct development. *J. Exp. Mar. Biol. Ecol.,* **150,** 131–147, doi:10.1016/0022-0981(91)90111-9.

Mason, E., J. Molemaker, A. F. Shchepetkin, F. Colas, J. C. McWilliams, and P. Sangrà, 2010: Procedures for offline grid nesting in regional ocean models. *Ocean Modell.,* **35,** 1–15, doi:10.1016/j.ocemod.2010.05.007.

McWilliams, J. C., 2007: Irreducible imprecision in atmospheric and oceanic simulations. *Proc. Natl. Acad. Sci. USA,* **104,** 8709–8713, doi:10.1073/pnas.0702971104.

——, 2009: Targeted coastal circulation phenomena in diagnostic analyses and forecasts. *Dyn. Atmos. Oceans,* **48,** 3–15, doi:10.1016/j.dynatmoce.2008.12.004.

——, and J. M. Restrepo, 1999: The wave-driven ocean circulation. *J. Phys. Oceanogr.,* **29,** 2523–2540, doi:10.1175/1520-0485(1999)029<2523:TWDOC>2.0.CO;2.

——, ——, and E. M. Lane, 2004: An asymptotic theory for the interaction of waves and currents in coastal waters. *J. Fluid Mech.,* **511,** 135–178, doi:10.1017/S0022112004009358.

Münchow, A., and R. J. Chant, 2000: Kinematics of inner shelf motions during the summer stratified season off New Jersey. *J. Phys. Oceanogr.,* **30,** 247–268, doi:10.1175/1520-0485(2000)030<0247:KOISMD>2.0.CO;2.

Nam, S., and U. Send, 2011: Direct evidence of deep water intrusions onto the continental shelf via surging internal tides. *J. Geophys. Res.,* **116,** C05004, doi:10.1029/2010JC006692.

——, and ——, 2013: Resonant diurnal oscillations and mean alongshore flows driven by sea/land breeze forcing in the coastal Southern California Bight. *J. Phys. Oceanogr.,* **43,** 616–630, doi:10.1175/JPO-D-11-0148.1.

Nidzieko, N., and J. Largier, 2013: Inner shelf intrusions of offshore water in an upwelling system affect coastal connectivity. *Geophys. Res. Lett.,* **40,** 5423–5428, doi:10.1002/2013GL056756.

Olabarrieta, M., J. C. Warner, and N. Kumar, 2011: Wave-current interaction in Willapa Bay. *J. Geophys. Res.,* **116,** C12014, doi:10.1029/2011JC007387.

——, ——, B. Armstrong, J. B. Zambon, and R. He, 2012: Ocean–atmosphere dynamics during Hurricane Ida and Nor'Ida: An application of the coupled ocean–atmosphere–wave–sediment transport (COAWST) modeling system. *Ocean Modell.,* **43–44,** 112–137, doi:10.1016/j.ocemod.2011.12.008.

Omand, M. M., J. J. Leichter, P. J. S. Franks, A. J. Lucas, R. T. Guza, and F. Feddersen, 2011: Physical and biological processes underlying the sudden appearance of a red-tide surface patch in the nearshore. *Limnol. Oceanogr.,* **56,** 787–801, doi:10.4319/lo.2011.56.3.0787.

——, F. Feddersen, P. J. S. Franks, and R. T. Guza, 2012: Episodic vertical nutrient fluxes and nearshore phytoplankton blooms in Southern California. *Limnol. Oceanogr.,* **57,** 1673–1688, doi:10.4319/lo.2012.57.6.1673.

O'Reilly, W., and R. T. Guza, 1991: Comparison of spectral refraction and refraction-diffraction wave models. *J. Waterw. Port Coastal Ocean Eng.,* **117,** 199–215, doi:10.1061/(ASCE)0733-950X(1991)117:3(199).

——, and ——, 1993: A comparison of two spectral wave models in the Southern California Bight. *Coastal Eng.,* **19,** 263–282, doi:10.1016/0378-3839(93)90032-4.

Pawlowicz, R., B. Beardsley, and S. Lentz, 2002: Classical tidal harmonic analysis including error estimates in MATLAB using T_TIDE. *Comput. Geosci.,* **28,** 929–937, doi:10.1016/S0098-3004(02)00013-4.

Pineda, J., 1994: Internal tidal bores in the nearshore: Warm-water fronts, seaward gravity currents and the onshore transport of neustonic larvae. *J. Mar. Res.,* **52,** 427–458, doi:10.1357/0022240943077046.

——, 1999: Circulation and larval distribution in internal tidal bore warm fronts. *Limnol. Oceanogr.,* **44,** 1400–1414, doi:10.4319/lo.1999.44.6.1400.

Raymond, W. H., and H. Kuo, 1984: A radiation boundary condition for multi-dimensional flows. *Quart. J. Roy. Meteor. Soc.,* **110,** 535–551, doi:10.1002/qj.49711046414.

Reeves, R. L., S. B. Grant, R. D. Mrse, C. M. C. Oancea, B. F. Sanders, and A. B. Boehm, 2004: Scaling and management of fecal indicator bacteria in runoff from a coastal urban watershed in Southern California. *Environ. Sci. Technol.,* **38,** 2637–2648, doi:10.1021/es034797g.

Reniers, A. J. H. M., J. A. Roelvink, and E. B. Thornton, 2004: Morphodynamic modeling of an embayed beach under wave group forcing. *J. Geophys. Res.,* **109,** C01030, doi:10.1029/2002JC001586.

——, J. H. MacMahan, E. B. Thornton, T. P. Stanton, M. Henriquez, J. W. Brown, J. A. Brown, and E. Gallagher, 2009: Surf zone surface retention on a rip-channeled beach. *J. Geophys. Res.,* **114,** C10010, doi:10.1029/2008JC005153.

Rippy, M. A., P. J. S. Franks, F. Feddersen, R. T. Guza, and D. F. Moore, 2013: Factors controlling variability in nearshore fecal pollution: Fecal indicator bacteria as passive particles. *Mar. Pollut. Bull.,* **66,** 151–157, doi:10.1016/j.marpolbul.2012.09.030.

Ris, R., L. Holthuijsen, and N. Booij, 1999: A third-generation wave model for coastal regions: 2. Verification. *J. Geophys. Res.,* **104,** 7667–7681, doi:10.1029/1998JC900123.

Romero, L., Y. Uchiyama, J. C. Ohlmann, J. C. McWilliams, and D. A. Siegel, 2013: Simulations of nearshore particle-pair dispersion in Southern California. *J. Phys. Oceanogr.,* **43,** 1862–1879, doi:10.1175/JPO-D-13-011.1.

Ruessink, B. G., J. R. Miles, F. Feddersen, R. T. Guza, and S. Elgar, 2001: Modeling the alongshore current on barred beaches. *J. Geophys. Res.,* **106,** 22 451–22 463, doi:10.1029/2000JC000766.

Sclavo, M., A. Benetazzo, S. Carniel, A. Bergamasco, and F. Falcieri, 2013: Wave-current interaction effect on sediment dispersal in a shallow semi-enclosed basin. *J. Coastal Res.,* **65,** 1587–1592.

Shanks, A. L., S. G. Morgan, J. MacMahan, and A. J. Reniers, 2010: Surf zone physical and morphological regime as determinants of temporal and spatial variation in larval recruitment. *J. Exp. Mar. Biol. Ecol.,* **392,** 140–150, doi:10.1016/j.jembe.2010.04.018.

Shchepetkin, A. F., and J. C. McWilliams, 2005: The Regional Oceanic Modeling System (ROMS): A split-explicit, free-surface, topography-following-coordinate oceanic model. *Ocean Modell.,* **9,** 347–404, doi:10.1016/j.ocemod.2004.08.002.

——, and ——, 2009: Correction and commentary for ''Ocean forecasting in terrain-following coordinates: Formulation and skill assessment of the regional ocean modeling system'' by Haidvogel et al., J. Comp. Phys. 227, pp. 3595–3624. *J. Comput. Phys.,* **228,** 8985–9000, doi:10.1016/j.jcp.2009.09.002.

Shearman, R. K., and S. J. Lentz, 2003: Dynamics of mean and subtidal flow on the New England shelf. *J. Geophys. Res.,* **108,** 3281, doi:10.1029/2002JC001417.

Sinnett, G., and F. Feddersen, 2014: The surf zone heat budget: The effect of wave breaking. *Geophys. Res. Lett.,* **41,** 7217–7226, doi:10.1002/2014GL061398.

Spydell, M. S., F. Feddersen, and R. T. Guza, 2009: Observations of drifter dispersion in the surfzone: The effect of sheared alongshore currents. *J. Geophys. Res.,* **114,** C07028, doi:10.1029/2009JC005328.

Suanda, S. H., J. A. Barth, R. A. Holman, and J. Stanley, 2014: Shore-based video observations of nonlinear internal waves across the inner shelf. *J. Atmos. Oceanic Technol.,* **31,** 714–728, doi:10.1175/JTECH-D-13-00098.1.

Thornton, E. B., and R. T. Guza, 1983: Transformation of wave height distribution. *J. Geophys. Res.,* **88,** 5925–5938, doi:10.1029/JC088iC10p05925.

——, and C. S. Kim, 1993: Longshore current and wave height modulation at tidal frequency inside the surf zone. *J. Geophys. Res.,* **98,** 16 509–16 519, doi:10.1029/93JC01440.

Tilburg, C., 2003: Across-shelf transport on a continental shelf: Do across-shelf winds matter? *J. Phys. Oceanogr.,* **33,** 2675–2688, doi:10.1175/1520-0485(2003)033<2675:ATOACS>2.0.CO;2.

Uchiyama, Y., J. C. McWilliams, and A. F. Shchepetkin, 2010: Wave-current interaction in an oceanic circulation model with a vortex-force formalism: Application to the surf zone. *Ocean Modell.,* **34,** 16–35, doi:10.1016/j.ocemod.2010.04.002.

——, E. Y. Idica, J. C. McWilliams, and K. D. Stolzenbach, 2014: Wastewater effluent dispersal in Southern California bays. *Cont. Shelf Res.,* **76,** 36–52, doi:10.1016/j.csr.2014.01.002.

Warner, J. C., N. Perlin, and E. D. Skyllingstad, 2008a: Using the model coupling toolkit to couple earth system models. *Environ. Modell. Software,* **23,** 1240–1249, doi:10.1016/j.envsoft.2008.03.002.

——, C. R. Sherwood, R. P. Signell, C. K. Harris, and H. G. Arango, 2008b: Development of a three-dimensional, regional, coupled wave, current, and sediment-transport model. *Comput. Geosci.,* **34,** 1284–1306, doi:10.1016/j.cageo.2008.02.012.

——, B. Armstrong, R. He, and J. B. Zambon, 2010: Development of a coupled ocean–atmosphere–wave–sediment transport (COAWST) modeling system. *Ocean Modell.,* **35,** 230–244, doi:10.1016/j.ocemod.2010.07.010.

Winant, C. D., and C. E. Dorman, 1997: Seasonal patterns of surface wind stress and heat flux over the Southern California Bight. *J. Geophys. Res.,* **102,** 5641–5653, doi:10.1029/96JC02801.

Wong, S. H. C., A. E. Santoro, N. J. Nidzieko, J. L. Hench, and A. B. Boehm, 2012: Coupled physical, chemical, and microbiological measurements suggest a connection between internal waves and surf zone water quality in the Southern California Bight. *Cont. Shelf Res.,* **34,** 64–78, doi:10.1016/j.csr.2011.12.005.